CHALMERS

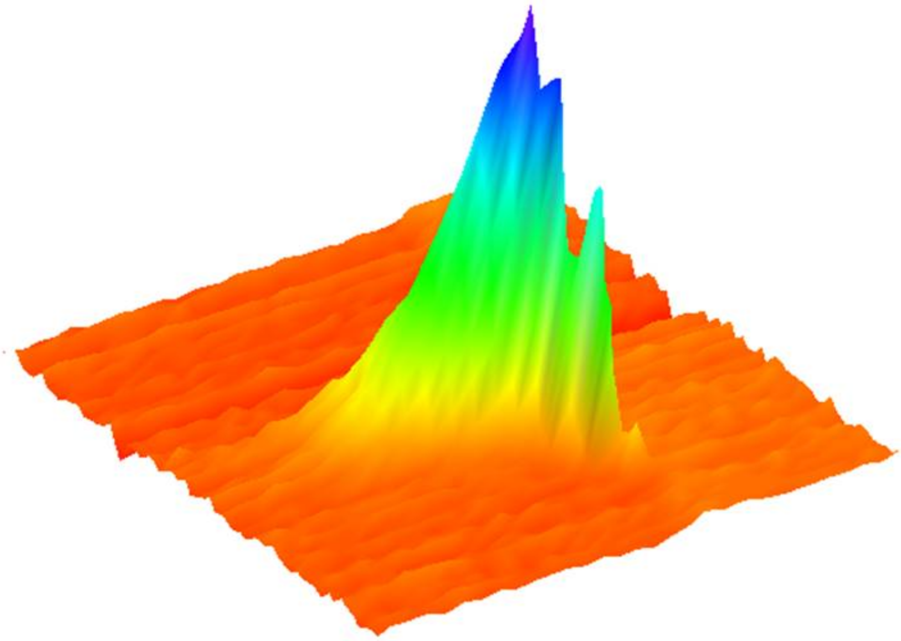

Photon Generation in a Doubly Tunable Resonator

Master's Thesis in Nanoscale Science and Technology

IDA-MARIA SVENSSON

Department of Microtechnology & Nanoscience
Quantum Device Physics Laboratory
CHALMERS UNIVERSITY OF TECHNOLOGY
Gothenburg, Sweden 2012

Photon Generation in a Doubly Tunable Resonator

Thesis for the degree Master of Science

IDA-MARIA SVENSSON

Department of Microtechnology & Nanoscience
Quantum Device Physics Laboratory
Chalmers University of Technology
Gothenburg, Sweden 2012

Photon Generation in a Doubly Tunable Resonator
Thesis for the degree Master of Science in Nanoscale Science and Technology
IDA-MARIA SVENSSON

Quantum Device Physics Laboratory
Department of Microtechnology & Nanoscience
Chalmers University of Technology
SE-412 96 Gothenburg, Sweden
Telephone:+46 (0)31 772 1000

Supervisor and examiner:
Prof. Per Delsing
Telephone:+46 (0)31 772 3317

Cover: Radiation generated by modulating two mirrors placed opposite of each other. This measurement is taken in the breathing mode when the two mirrors oscillate symmetrically around a center point and the distance between them is changing with time.

Printed at Chalmers Reproservice
Gothenburg, Sweden 2012

Photon Generation in a Doubly Tunable Resonator
IDA-MARIA SVENSSON
Department of Microtechnology & Nanoscience
CHALMERS UNIVERSITY OF TECHNOLOGY

Abstract

In November 2011 the first experimental observation of the dynamical Casimir effect was published [1]. Superconducting circuits were used to show that a single mirror moving in vacuum could generate photons, by parametric amplification of vacuum fluctuations. This project is a side track of this research where a second mirror is introduced to investigate photon generation in-between the mirrors. The work includes both theory studies and experimental practice. Resonators have been fabricated on chip in a cleanroom and measured in a dilution refrigerator. The focus has been on how the different boundary conditions of the resonator field affect the photon generation.

A superconducting circuit has been used including a $\lambda/2$ resonator with two SQUIDs inducing tunability of the resonance frequency via on-chip flux tuning lines. The two SQUIDs are placed in each end of the cavity in order to simulate moving mirrors. The mirrors are used to modulate the boundary conditions of the cavity. This is done by changing the SQUID inductance which is achieved by applying a magnetic flux to the SQUID loop. Depending on if the mirrors move in or out of phase, a breathing or translational mode can be created in the cavity. Theory predicts photon generation in different modes depending on if the pump frequency is two or three times the resonance frequency [2].

Measurements have been done at a temperature of around 50 mK, which is low enough to have a negligible amount of thermal photons and quasi-particles in the cavity. The static tuning of the resonator have been probed by sweeping the fluxes applied to the two SQUIDs and at each point the resonance frequency has been extracted. Good results have been achieved and two dimensional tuning is shown.

A high frequency, flux modulation have been applied to the SQUIDs both one at a time and simultaneously to generate photons. In the two mirror modulation case qualitative agreement with theory has been observed for driving in the breathing and translational mode respectively. Generation occurs first for the breathing mode at 2ω (twice the resonance frequency) and for the translational mode at 3ω.

Acknowledgements

First of all I want to thank my supervisor and examiner professor Per Delsing for trusting me with this challenging project. It has been encouraging to work as a pioneer with experiments that have not been tried before. Thanks to this opportunity I finally realized the glory of physics and its possibilities. I have during this year learned that a graph tells you something, it is not some lines here and there, it tells a story.

I would also like to thank my supervisors: Mathieu Pierre, you have been a terrific teacher, teaching me everything from cleanroom fabrication and quantum physics to English grammar and Michaël Simoen, thank you for all the time you spent in the lab helping me with measurements and answering my questions. In addition, apart from the more scientific work I would like to thank both of you for all the laughs, jokes and interesting discussions during the days in the lab!

Thank you QDP for a great year! I will be for ever grateful for how I from the first day was welcomed to the group and how you have all taken care of me. QDP is a great research group with a wonderful atmosphere and it is an honor to be part of it!

Also I want to thank my fellow engineering physics friends for many enjoyable lunches in Signes and to Maria and Louise for many needed coffee breaks and walks. Chalmers would not be the same without you.

And finally Simon, thank you for being the supporting and caring person you are!

Ida-Maria, Göteborg May, 2012

Contents

1

Introduction

Nanotechnology provides researchers with a possibility of observing physical phenomena on a small scale, which in turn allows studies of more complicated systems such as quantum mechanical systems. One example of what is treated in such a system is the interaction between light and matter. In the field of circuit Quantum ElectroDynamics (circuit-QED) electrical circuits are used as platforms for this interaction and quantum mechanical effects previously only predicted theoretically can be shown. This means that thought experiments involving single atoms or photons can be realized. An advantage of using electrical circuits with one dimensional structures and microwaves instead of three dimensional optical systems is that the characteristics of the systems are tailorable and a strong light-matter interaction can be achieved. Another advantage is that the microwave circuit can be fabricated on-chip and integrated with many other circuits.

One phenomena that can be investigated using circuit-QED is the dynamical Casimir effect, which is a quantum field theory phenomenon. Although suggested 40 years ago it was only recently observed [1]. The idea with this thesis is to simulate and measure photon generation in a doubly tunable resonator, a system which has been well studied theoretically [2, 3, 4]. An observation of photon generation in a doubly tunable resonator is a step towards observing the dynamical Casimir effect in the same system.

1.1 The Casimir Effect

Imagine two ideal mirrors (perfectly conducting uncharged plates) placed in space (vacuum) opposite to each other. If placed at a very short distance, they will attract each other by a force known as the Casimir force [5]. This force appears because the distance between the mirrors limits the number of electromagnetic modes between them and this limited number is much smaller than the number of modes outside the mirrors, which implies a radiation pressure on them. Because of a higher pressure from the outside than the inside, this force is attractive, which is illustrated in Fig. 1.1.

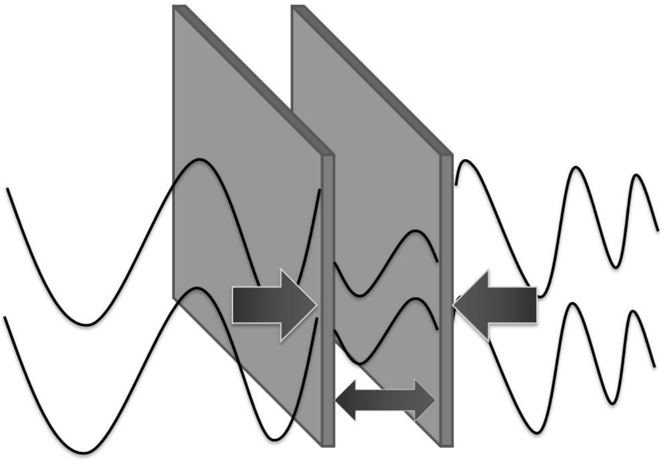

Figure 1.1: An illustration of the Casimir effect, the vacuum fluctuations exert a force to the mirrors.

Moving the mirrors, *i.e.* applying time-dependent boundary conditions to the field creates electromagnetic excitations in the modes between the mirrors. In turn these excitations act as an opposing force for the mirror movement. However, the motion has to be very fast. In fact, the velocity of the mirrors has to be close to the speed of light. In this process photons are created apparently out of nothing (vacuum) but at a closer look this is not the case. According to quantum mechanics the field between the mirrors is quantized. The energy is collected into small packages, photons. Even in the ground state of this quantized field, which is called vacuum, fluctuations occur [6]. These fluctuations are referred to as vacuum fluctuations or quantum fluctuations. Photons are created as a result of the interaction between vacuum fluctuations and the time-dependent boundary conditions [7]. This is called the dynamical Casimir effect [8]. It has also been shown that there is no requirement to have two mirrors to generate photons from vacuum fluctuations. A single mirror moving with a non-uniform acceleration can also generate radiation [9].

1.2 Previous Work

In order to measure the dynamical Casimir effect, previous studies have been done on various cavity setups. To generate photons the mirrors need to be moved with a speed close to the speed of light. With physical mirrors this needs to be performed mechanically which is extremely difficult. Instead an electrical circuit can be used to create the effect. In a superconducting resonator, the boundary conditions can be modulated using a Superconducting Quantum Interference Device (SQUID) [7]. The SQUID, behaving as a parametric inductance, is used to change the electrical length of the resonator and hence its resonance frequency. The resonator end is directly connected to ground, *i.e.* terminated with a very low impedance compared to the resonator characteristic impedance, which acts as a mirror for the field. When the SQUID is modulating the resonance frequency at a high speed, the imaginary mirror is moving with a speed close to the speed of light. It has been shown that the SQUID-terminated resonator can tune the field in a resonator faster than the photon lifetime [10]. This means that the frequency of the photons stored in the cavity is changed.

At Chalmers photon generation experiments have been done with SQUID-terminated $\lambda/4$ resonators [11]. Their results showed a generation of photons though it could not be concluded that it was exclusively from excitations of vacuum fluctuations. Recently new experiments were done with a different setup [1]. Instead of a resonator, a short aluminum coplanar waveguide was used, in which direct measurements of the photon generation was allowed. The analogy would be a single mirror moving in vacuum [12]. The experiment [1] is the first reported experimental verification of the dynamical Casimir effect.

1.3 Project Objectives

This thesis is a continuation of the research of Wilson *et al.* [11] with a focus on experimental verification of theories presented by several groups [2, 3, 4]. The system consists of a cavity with two movable mirrors, one in each end. The goal is to investigate the photon generation effect when changing the boundary conditions on both sides. With two mirrors both a breathing mode, when the mirrors oscillate symmetrically around the center of the cavity, and a translational mode, where the mirrors oscillate together and the distance between them is constant, can be created. Naively one would expect that both mirrors generate photons independently. This is the case when the two mirrors oscillate with different frequencies but driving the two mirrors with the same frequency gives rise to interference [2]. Considering the wave particle duality, the generated photons can be treated as particles bouncing back and forth between two walls. The relative motion of both the mirrors and the photons has to be taken into account.

In Fig. 1.2, the theoretical prediction is presented as space-time diagrams both for the breathing and translational modes. The sinusoidal curves represent the position of the mirrors in time. Assuming the same oscillation frequency of the two mirrors there are two interesting cases, driving the mirrors at two or three times the resonance frequency, the 2ω or 3ω-case. To create breathing and translational modes a phase offset between the two mirror motions is introduced. Further the mirrors can be assigned to move with an arbitrary phase difference and photon generation can be measured as a function of this phase.

Since superconducting circuits are used, the moving mirror is actually a modulation of the boundary conditions of the field inside the cavity. Photons are created as propagating excitations in this field [7]. Depending on if in the 2ω or 3ω-case, photon generation is predicted in different modes. In the 2ω-case constructive interference appears in the breathing mode, while the interference is destructive in the translational mode and no

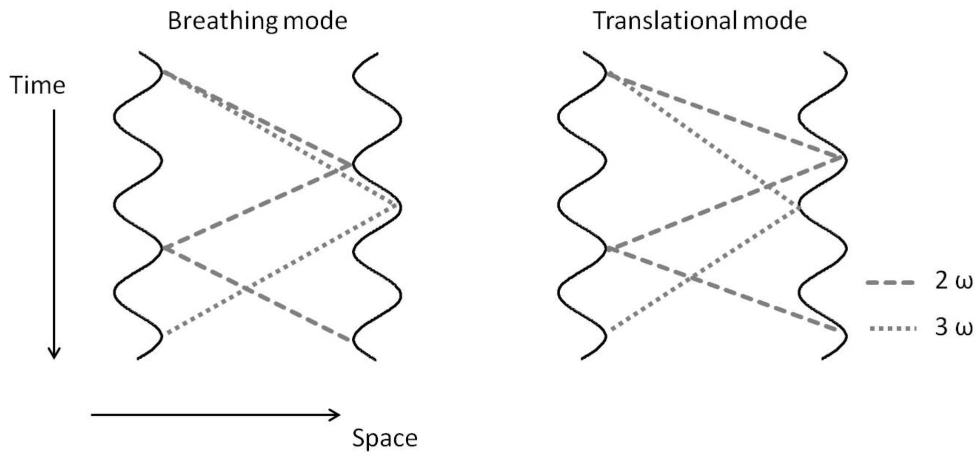

Figure 1.2: Space time diagrams of the mirror movement when they move in and out of phase, breathing and translational mode respectively.

photons are generated. However in the 3ω-case the inference is constructive in the translational mode and photons are generated and destructive in the breathing mode [2].

The objective of this thesis project was to design and fabricate a doubly tunable resonator. The tunability of the resonance frequency was tested and characterized. Driving the system with high frequency flux modulation the photon generation has been measured. Its dependence of parameters such as flux amplitude and driving frequency as well as phase offset between the driving signals has been investigated.

2

Theory

2.1 Introduction to Superconductivity

In 1911, Kammerling Onnes found the superconducting transition in mercury [13]. He observed a significant drop in electrical resistivity when cooling to liquid helium temperature. Short afterwards more metals were discovered to be superconducting. The temperature at which the transition occurs is called critical temperature and at this temperature the electrons start to form pairs, Cooper pairs. Two electrons attracting each other can be explained by the BCS theory as a result of the electron phonon interaction. In a crude picture electrons are very light and fast compared to heavy metal ions. When a fast electron is passing through a metal ion lattice, the slow but positively charged ions are attracted and moves closer together forming a positively charged area attracting another electron.

The superconductivity phenomenon is an effect arising from electron phonon coupling in the lattice. Therefore substances that are relatively good conductors at room temperature such as copper, silver and gold never undergoes a superconducting transition. Commonly used superconductor materials are aluminum and niobium, since they allow fabrication of small structures. Due to the very low resistivity at both low and high frequencies, superconductors allow for fabrication of low loss devices.

A special property of the superconductors are that the electron states are gathered in two bands separated by an energy gap. This energy gap is located symmetrically around the Fermi energy and is one of the reasons why superconductors have bad thermal conduction. Another property of superconductors are that they expel magnetic fields in the superconducting state. This is called the Meissner effect [14].

2.2 The Josephson Effect

Brian Josephson was the first one to theoretically predict the behavior of a tunneling current in a weak link between two bulk superconductors [15]. This theory has later been extended to hold not only for tunneling currents but for a variety of weak link junctions, commonly called Josephson junctions. These junctions are the most important building blocks for non-linear devices, which are used for creating energy spectras with non-equidistant energy level separation. Such energy spectras are called anharmonic and junctions allow for fabrication of systems with well defined energy levels, *i.e.* artificial atoms.

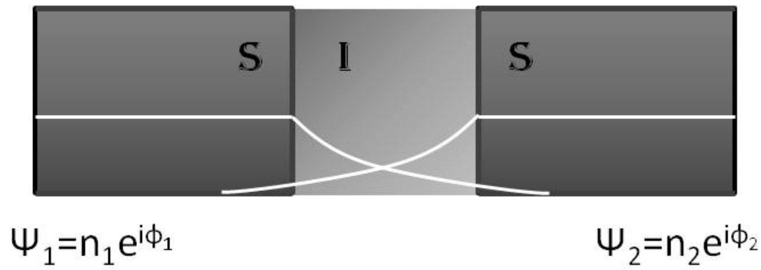

Figure 2.1: A SIS (superconductor-insulator-superconductor) junction. The white line indicates the BCS wavefunction extension, and the fact that the wavefunction reaches the other side of the junction allows for tunneling of Cooper pairs.

A regular Josephson junction consists of two superconducting contacts separated by a thin insulating layer, Fig. 2.1. The current flowing through the junction consists of tunneling Cooper pairs and depends on the phase difference of the wave functions on each side of the junction, $\varphi = \phi_2 - \phi_1$, as

$$I = I_c \sin\varphi, \tag{2.1}$$

which is known as the DC Josephson relation. I_c is the critical current, corresponding to the maximum current which the junction can support. The phase difference can be related to a voltage as

$$\frac{d\varphi}{dt} = \frac{2e}{\hbar}V. \tag{2.2}$$

This is the AC Josephson relation. In the junction an energy can be stored and expressed as

$$E_J = \frac{\hbar I_c}{2e}, \tag{2.3}$$

the Josephson energy. In addition the junction can behave as an inductor and the two parallel plates also form a capacitor. Depending on the frequency regime the capacitive or the inductive ability is stronger. For frequencies well below the plasma frequency $f_p = 1/2\pi\sqrt{LC}$ it behaves mostly as an inductor. Using that $V = L\frac{dI}{dt}$ and inserting the Josephson equations an inductance can be extracted as

$$L = \frac{\hbar}{2eI_c\cos\varphi}. \tag{2.4}$$

2.3 The SQUID

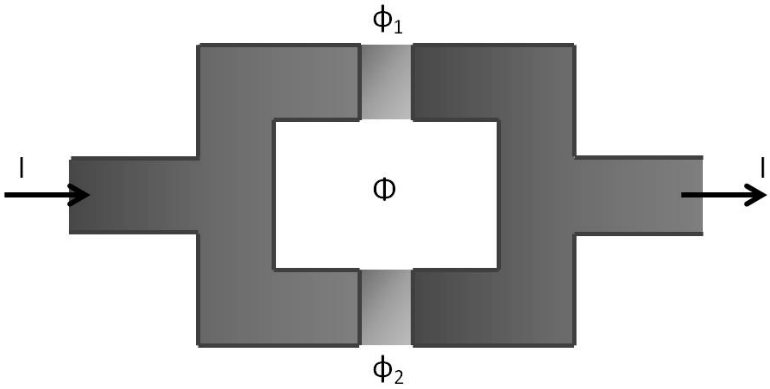

Figure 2.2: Two Josephson junctions in parallel form a SQUID, a sensitive magnetometer.

Two parallel Josephson junctions forming a loop are called a Superconducting Quantum Interference Device (SQUID), which can be used for very sensitive magnetic flux measurements [16]. It can also be used for modulation, in a cavity or a transmission line it can be used as a parametric inductance to tune the electrical length. By controlling the magnetic flux through the SQUID loop, the inductance is set and thereby the electrical length. Following notation of Fig. 2.2 and including the phase gradient,

$$\nabla\theta = -\delta\vec{J}_s - \frac{2e}{\hbar}\vec{A},$$

known from the derivation of the London equations [17], the SQUID inductance can be derived. θ corresponds to the superconducting phase, $\vec{J}_s$ the supercurrent, δ a constant and $\vec{A}$ the electromagnetic vector potential. Integrating over a closed loop and choosing a path well inside the conductor gives $\vec{J}_s = 0$, since supercurrents are only flowing on the surfaces. The integral can then be written

$$\oint \nabla\theta dl = -\oint \delta\vec{J}_s dl - \frac{2e}{\hbar}\oint \vec{A}dl$$

and then rewritten

$$2\pi n - \phi_1 + \phi_2 = 0 - \frac{2e}{\hbar}\int \nabla\times\vec{A}dS = -\frac{2e}{\hbar}\int \vec{B}dA = -\frac{2e}{\hbar}\Phi.$$

Introducing the flux quanta $\Phi_0 = \frac{h}{2e}$ this can be rewritten again as

$$\phi_1 - \phi_2 = 2\pi n + 2\pi\frac{\Phi}{\Phi_0}.$$

Assuming Φ sweeping over the whole range the n term can be ignored. The total current flowing in the SQUID, assuming identical junctions $I_{c_1} = I_{c_2} = I_c$, is

$$I = I_c(\sin\phi_1 + \sin\phi_2),$$

which can be rewritten

$$I = 2I_c \sin\varphi |\cos\frac{\phi_1 - \phi_2}{2}| = 2I_c \sin\varphi |\cos\frac{\pi\Phi}{\Phi_0}|,$$

here $\varphi = \frac{\phi_1+\phi_2}{2}$. This resembles the DC Josephson relation for a single junction. From this and remembering the AC Josephson relation, the SQUID inductance can be calculated while $V = L\frac{dI}{dt}$, which yields

$$L_s = \frac{\hbar}{4eI_c \underbrace{|\cos\frac{\pi\Phi}{\Phi_0}|}_{\text{tunability}}} \frac{1}{\underbrace{\cos\varphi}_{\text{non-linearity}}}. \tag{2.5}$$

If we assume that the current flowing through the junctions is much smaller than the SQUID critical current, φ is small and $\cos\varphi \approx 1$.

2.4 Resonators

Entering the superconducting regime, many microwave components benefit highly from the decreased losses [16]. One of these is the microwave resonator, which simply consists of a finite length transmission line. This transmission line can store energy as oscillating standing waves. Standing waves imply that only certain discrete energy values are allowed, *i.e.* the set of modes in the energy spectra is discrete [18].

One transmission line of the planar type is the CoPlanar Waveguide (CPW) [19]. It consists of a center conductor capacitively coupled to a ground plane via a gap, as shown in Fig. 2.3. Compared to other types of transmission lines, the CPW is convenient to fabricate in small scales at the surface of a chip.

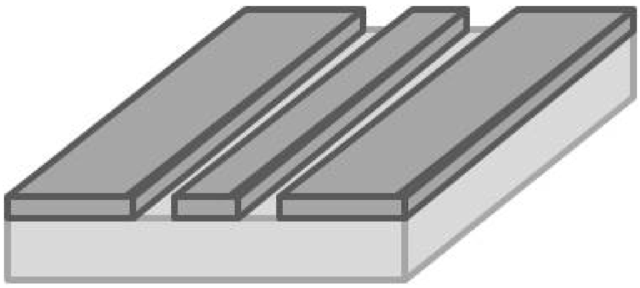

Figure 2.3: A coplanar waveguide is a planar transmission line structure including a center conductor capacitively coupled to the ground planes.

The resonator is characterized by its resonance frequency, at which the stored energy oscillates between its capacitive and inductive forms, and a quality factor, which is a measure of the losses in a resonator. It can be defined as

$$Q = \frac{\text{Stored energy}}{\text{Dissipated energy/radian}}.$$

The total Q value describes both internal losses, losses inside the resonator and external losses due to the coupling between the resonator and the outside world. The relation can be written

$$\frac{1}{Q} = \frac{1}{Q_{ext}} + \frac{1}{Q_{int}}. \tag{2.6}$$

Experimentally the Q value can be determined from a reflection or transmission measurement studying the resonance linewidth as

$$Q = \frac{f_r}{\Delta f}, \tag{2.7}$$

where f_r is the resonance frequency and Δf is the full width half maximum of the resonance. This is only valid when Q_{int} is different from Q_{ext}.

2.4.1 Lumped Element Model

A transmission line resonator can be modeled as a lumped element circuit with an inductance, a capacitance and a resistance. The resistance represents internal losses in the resonator. In Fig. 2.4 an equivalent circuit schematic is presented for a lumped element resonator capacitively coupled to a transmission line. The resonance frequency

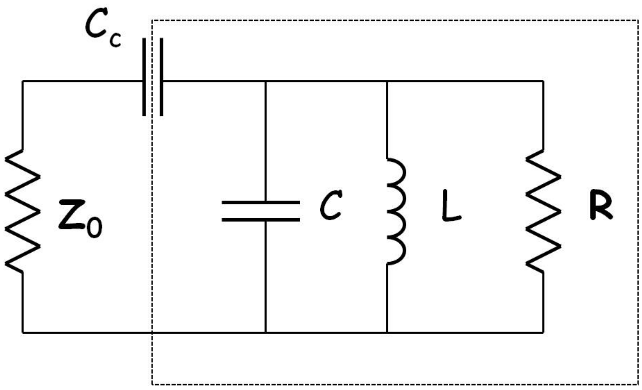

Figure 2.4: Using lumped element method a transmission line resonator can be modeled as a capacitance, inductance and resistance in parallel. C_c indicates the coupling between the resonator and the outside world and Z_0 is the characteristic impedance.

is given by

$$\omega_r \approx \frac{1}{\sqrt{L(C + C_c)}}, \tag{2.8}$$

and following the thesis of Sandberg [20] the Q values can be expressed

$$Q_{int} = \frac{\omega_r RC((\omega_r C_c Z_0)^2 + 1 + C_c/C)}{(\omega_r C_c Z_0)^2 + 1}, \tag{2.9a}$$

$$Q_{ext} = \frac{((\omega_r C_c Z_0)^2 + 1)C + C_c}{Z_0 C_c^2 \omega_r}. \tag{2.9b}$$

Using the assumption that the coupling is small $\omega_r C_c Z_0 \ll 1$, equations (2.9a) and (2.9b) can be rewritten as

$$Q_{int} = \omega_r R(C + C_c), \tag{2.10a}$$

$$Q_{ext} = \frac{C + C_c}{\omega_r C_c^2 Z_0}. \tag{2.10b}$$

2.4.2 Calculation of the Reflection Coefficient

Comparing incoming and outgoing signals for the resonator an expression for the reflection coefficient can be given as follows [18]

$$\Gamma = \frac{Z_L - Z_0}{Z_L + Z_0}, \tag{2.11}$$

where Z_L is the load impedance of the circuit and Z_0 is the characteristic impedance of the transmission line. To simplify calculations the resonator lumped element model can be modified to the circuit diagram in Fig. 2.5. The coupling capacitance C_c and impedance Z_0 have been replaced by equivalent parallel elements

$$\tilde{Z}_0 = \frac{1}{\omega_r^2 Z_0 C_c^2} \text{ and } \tilde{C}_c \approx C_c.$$

The external Q value can for this circuit be written $Q_{ext} = \omega_r \tilde{Z}_0(C + C_c)$. The load

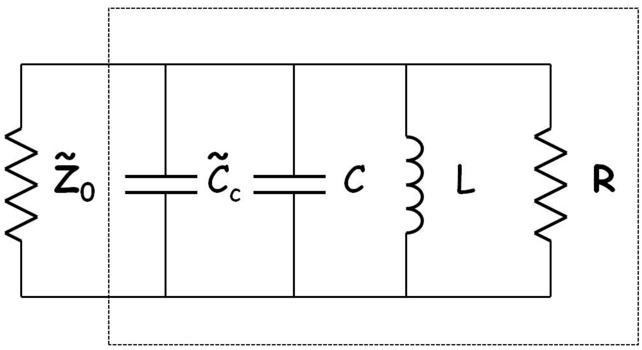

Figure 2.5: The characteristic impedance and coupling capacitance from the circuit diagram in Fig. 2.4 have been replaced by equivalent parallel ones in order to simplify calculations.

admittance of the resonator modeled as a lumped element circuit with parallel elements can then be expressed as

$$Y_L = \frac{1}{Z_L} = \frac{1}{R} + i\omega(C + C_c) + \frac{1}{i\omega L},$$

which can be rewritten

$$Y_L = \frac{1}{R} + i\omega(C + C_c)\left(1 - \frac{1}{\omega^2 L(C + C_c)}\right).$$

Inserting (2.8) gives

$$Y_L = \frac{1}{R} + i\omega(C + C_c)\left(1 - \frac{\omega_r^2}{\omega^2}\right),$$

where the last part can be simplified as

$$\left(1 - \frac{\omega_r^2}{\omega^2}\right) = \frac{\omega^2 - \omega_r^2}{\omega^2} = \frac{\overbrace{(\omega - \omega_r)}^{=\Delta\omega}(\omega + \omega_r)}{\omega^2} = \frac{\Delta\omega}{\omega}\left(1 + \frac{\omega_r}{\omega}\right) = \frac{\Delta\omega}{\omega}\left(1 + \frac{1}{1 + \frac{\Delta\omega}{\omega_r}}\right) \approx 2\frac{\Delta\omega}{\omega},$$

since it can be assumed that $\Delta\omega \ll \omega_r$, working around the resonance frequency. Hence

$$Y_L = \frac{1}{R} + 2i\underbrace{(C + C_c)}_{=\frac{Q_{int}}{\omega_r R}}\Delta\omega = \frac{1}{R} + i\frac{2\Delta\omega Q_{int}}{\omega_r R},$$

using (2.10a). To simplify further calculations it is noticed that (2.11) can be rewritten

$$\Gamma = \frac{\tilde{Y}_0 - Y_L}{\tilde{Y}_0 + Y_L},$$

where $\tilde{Y}_0 = 1/\tilde{Z}_0$. When inserting the expression for the load admittance the resulting expression is

$$\Gamma = \frac{\frac{1}{\tilde{Z}_0} - \frac{1}{R} - i\frac{2\Delta\omega Q_{int}}{\omega_r R}}{\frac{1}{\tilde{Z}_0} + \frac{1}{R} + i\frac{2\Delta\omega Q_{int}}{\omega_r R}} = \frac{\frac{R}{\tilde{Z}_0} - 1 - i2Q_{int}\frac{\Delta\omega}{\omega_r}}{\frac{R}{\tilde{Z}_0} + 1 + i2Q_{int}\frac{\Delta\omega}{\omega_r}}$$

and using $\frac{R}{\tilde{Z}_0} = \frac{Q_{int}}{Q_{ext}}$, the result is

$$\Gamma = \frac{\frac{1}{Q_{ext}} - \frac{1}{Q_{int}} - 2i\frac{\Delta\omega}{\omega_r}}{\frac{1}{Q_{ext}} + \frac{1}{Q_{int}} + 2i\frac{\Delta\omega}{\omega_r}}, \tag{2.12}$$

where $\Delta\omega = \omega - \omega_r$ is the detuning.

Depending on how the internal and external losses in the resonator compare to each other, the resonator can be in different regimes. When $Q_{ext} > Q_{int}$ the resonator is undercoupled and this implies that more energy is lost inside the resonator than in the coupling to other circuitry. If $Q_{int} > Q_{ext}$, more energy is lost through the coupling than inside and the resonator is said to be overcoupled instead. At the critical point were $Q_{int} = Q_{ext}$, the resonator is critically coupled. Depending on the measurements different regimes are preferable. Obviously if the resonator is undercoupled the signal that can be measured might be low since more is lost inside than comes out. If over-coupled, the resonance is always visible, although if strongly overcoupled the resonator is highly damped. The optimum to measure reflection is usually to work around critical coupling, while in this regime the resonator is visible but still able to store energy.

2.4.3 Tuning Frequency Model

The circuit investigated in this thesis, a $\lambda/2$ resonator with a SQUID in each end can be translated into the transmission line model in Fig. 2.6, assuming that the $\lambda/2$ resonator is formed by two $\lambda/4$ resonators. Using transmission line theory an expression can be calculated for the tuned resonance frequency as follows.

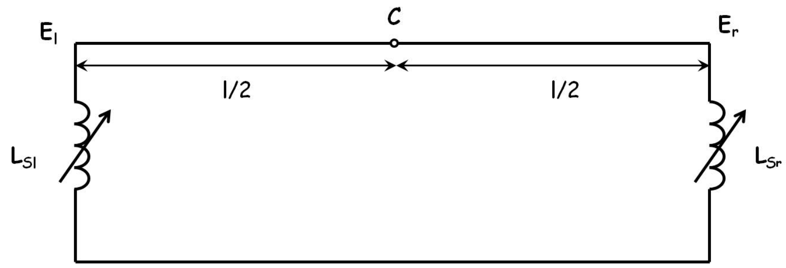

Figure 2.6: A transmission line model of the system in figure 3.1. The $\lambda/2$ resonator is assumed to be equivalent to two $\lambda/4$ resonators. The physical length of the resonator is denoted l.

This theory gives a relationship for reflection and impedance as

$$\Gamma = \frac{Z - Z_0}{Z + Z_0} \text{ and } Z = Z_0 \frac{1+\Gamma}{1-\Gamma}.$$

In this case the load is the tunable inductances $Z_L = i\omega L_s$ and assuming no losses, the propagation between the center point C and endpoint E can be modeled

$$V^+(E_{l/r}) = e^{-ik\frac{l}{2}} V^+(C),$$

$$V^-(C) = e^{-ik\frac{l}{2}} V^-(E_{l/r}),$$

as forwards and backwards propagating signals. The center point C is where the coupling capacitance is connected. The coupling induces a small shift in resonance frequency that is neglected here, assuming it is small. Using this, the reflection in one of the resonator ends can be written

$$\Gamma_{l/r} = \Gamma_L^{l/r} e^{-ikl} = \frac{Z_L^{l/r} - Z_0}{Z_L^{l/r} + Z_0} e^{-ikl}.$$

Rewriting as an impedance

$$Z_{l/r} = Z_0 \frac{1+\Gamma_{l/r}}{1-\Gamma_{l/r}}, \tag{2.13}$$

the circuit schematic in Fig. 2.6 can be redrawn as the simpler circuit in Fig. 2.7 consisting of two impedances. According to Kirchhoffs voltage law the voltages around the loop add up to zero, hence

$$Z_l + Z_r = 0.$$

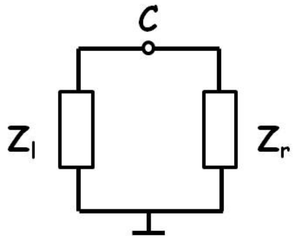

Figure 2.7: A simplification of the model in Fig. 2.6.

Inserting equation (2.13) gives the condition

$$\Gamma_l \Gamma_r = 1,$$

which can be written

$$\frac{i\omega L_s^l - Z_0}{i\omega L_s^l + Z_0} e^{-ikl} \frac{i\omega L_s^r - Z_0}{i\omega L_s^r + Z_0} e^{-ikl} = 1.$$

For resonance to occur this equation needs to be satisfied, which it is if the sum of the phases on the left hand side ads up to the phases on the right hand side, which implies

$$2\pi n - 2\arctan\frac{\omega L_s^l}{Z_0} - 2\arctan\frac{\omega L_s^r}{Z_0} = 2kl.$$

Assuming $\omega L_s \ll Z_0$, $\arctan\frac{\omega L_s}{Z_0} \approx \frac{\omega L_s}{Z_0}$ and the resulting expression for the resonance frequency is

$$\omega = \frac{n\pi v/l}{1 + \frac{L_s^l v}{Z_0 l} + \frac{L_s^r v}{Z_0 l}} = \frac{f_0}{1 + \frac{L_s^l}{L_l l} + \frac{L_s^r}{L_l l}}, \qquad (2.14)$$

where $k = \frac{\omega}{v}$ has been included (v is the speed of light in the resonator) [18]. Further rewriting has been made using $Z_0 = \sqrt{L_l/C_l}$ and $v = 1/\sqrt{L_l C_l}$, which gives $\frac{v}{Z_0} = \frac{1}{L_l}$. $n\pi v/l$ can be called the base frequency f_0, which is the resonance frequency of the resonator without SQUIDs. Instead of resonance frequency the resonator can be characterized by its wavelength, λ, using the relation

$$\lambda = 2\pi v/\omega.$$

In the simplest case the two SQUIDs are treated separately with two separate fluxes coming from respective fluxline. If instead the flux corresponding to one of the SQUIDs also affects the other one, a crosstalk between the SQUIDs is visible. The argument of the SQUID inductance then changes from $L_s = \frac{L_{s0}}{\cos\frac{\pi\Phi_{ext}}{\Phi_0}}$ to

$$L_s = \frac{L_{s0}}{\cos\frac{\pi(\Phi_{ext} - \Phi_{ct})}{\Phi_0}},$$

where Φ_{ct} corresponds to the amount of flux leaking from the opposite tuning line.

2.5 Parametric Oscillators

A parametric oscillator [21] is a non-linear system in which one or more parameters can be varied in time. The oscillating parameter can be for instance the resonance frequency or the damping and is modulated by an external pump. In the tunable resonator case [10], the resonance frequency is modulated by a flux applied to the SQUID loop. When pumping the flux at twice the resonance frequency, the resonator amplitude exponentially increases in time [11], although there is a saturation limit caused by non-linearities in the system. If there are losses in the system and hence damping there exists a threshold above which the exponential growth starts. In the region right below the threshold the parametric oscillator can be used as a parametric amplifier. A small signal sent into the resonator at half the pump frequency, when pumping around twice the resonance frequency, will then be amplified.

The parametric amplifier can be explained as a parametric oscillator with an input signal driven in a certain regime. If driving this parametric amplifier in a one dimensional resonator with a zero temperature vacuum groundstate by changing the boundary conditions of the resonator field, the dynamical Casimir effect is present. The condition for having the dynamical Casimir effect is that the amplified signal originates from vacuum fluctuations which are only present if the system is in the quantum mechanical regime. To ensure the absence of thermal fluctuations the temperature needs to be significantly lower than the oscillator frequency $k_B T \ll \hbar\omega$. At a higher temperature the cavity would apart from vacuum fluctuations also contain thermal noise that also can be amplified by a parametric amplifier but does not imply the dynamical Casimir effect [7, 22].

3

Design

In Fig. 3.1, a schematic setup of this experiment can be seen. The main features can be identified as two identically designed SQUIDs connected on each side of a coplanar waveguide $\lambda/2$ resonator, and a coupling capacitance in the middle to enable probing.

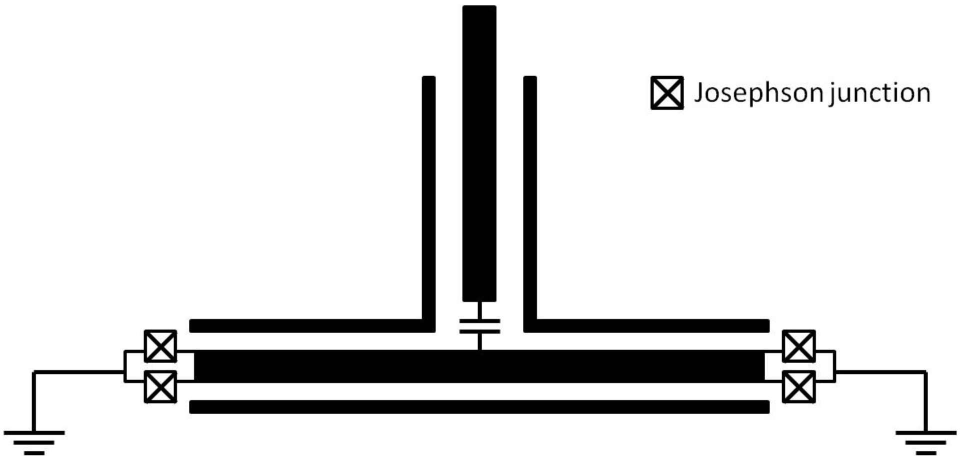

Figure 3.1: A schematic illustration of the doubly tunable cavity. The horizontal part is the resonator with one SQUID in each end. Measurements are done in the middle via the capacitively coupled transmission line.

3.1 The Resonator

The circuit is fabricated in aluminum and the coplanar waveguide dimensions were decided to be $w = 10\,\mu$m center conductor width and $s = 6\,\mu$m gap width, since these are dimensions that match to a $50\,\Omega$ characteristic impedance. Using the Microwave office tool TXline and assuming a $\lambda/2$ resonator with $50\,\Omega$ characteristic impedance gives a resonator length of around 12 mm wishing a resonance frequency around 5 GHz.

From Göppl *et al.* [23] a capacitance and inductance per unit length of the resonator can be calculated as

$$L_l = \frac{\mu_0}{4}\frac{K(k_0')}{K(k_0)} = 4.4 \cdot 10^{-7}\,\mathrm{H/m} \text{ and} \tag{3.1a}$$

$$C_l = 4\epsilon_0\epsilon_{eff}\frac{K(k_0)}{K(k_0')} = 1.6 \cdot 10^{-10}\,\mathrm{F/m}. \tag{3.1b}$$

K is the complete elliptic integral of the first kind where k_0 and k_0' are geometry parameters,

$$k_0 = \frac{w}{w+2s},$$

$$k_0' = \sqrt{1-k_0^2},$$

where w is the width of the center conductor and s the width of the gap. ϵ_0 is the permittivity of free space and ϵ_{eff} is the effective relative permittivity of the dielectric of the coplanar waveguide. The dielectric is the substrate material, silicon with a thin layer of silicon oxide on top and air above. This gives an ϵ_{eff} around 6.2. From (3.1a) and (3.1b) the impedance of the line can be calculated as

$$Z_0 = \sqrt{\frac{L_l}{C_l}} = 52.4\,\Omega,$$

which is close enough to the desired characteristic impedance $50\,\Omega$. The speed of light in a medium is $v_{photon} = \frac{1}{\sqrt{\mu\epsilon}}$. Silicon and silicon oxide as well as air are non-magnetic substances, thus $\mu = \mu_0$. Then the light velocity in this resonator can be calculated as

$$v_{photon} = \frac{1}{\sqrt{\mu_0\epsilon_0\epsilon_{eff}}} = \frac{1}{\sqrt{L_lC_l}} = 1.19 \cdot 10^8\,\mathrm{m/s}.$$

This gives that the light speed in the cavity corresponds to around 40 % of the speed of light in vacuum.

3.2 Circuit Elements Design

Each end of the resonator is terminated by a SQUID. Following the results of Sandber [20], a critical current of around $1-2\,\mu A$ is aimed for to have a good tunability. The SQUID normal resistance is calculated as [24]

$$R_N = \frac{R_Q\Delta}{2E_J},$$

where $R_Q = \frac{h}{4e^2}$ is the superconducting resistance quantum and E_J the Josephson energy (2.3). Δ is the superconducting energy gap and can according to the BCS theory be written $\Delta = 1.76 k_B T_c$, where k_B is Boltzmann constant and T_c for thin film aluminum is 1.4 K. These assumptions give a SQUID resistance of $170 - 330\,\Omega$. To obtain a specific resistance the free parameters are the oxide layer thickness and the area of the junction surface. Using the SQUID design guide of Krantz [25] a resistance of $208\,\Omega$ can be reached by choosing junction dimensions as $0.25 \times 2\,\mu$m and an oxidation time of 30 min at a pressure of 0.2 mbar corresponding to around 1 nm thickness. These parameters also require an evaporation angle of $26.5°$, which will be explained in more detail in chapter 4.

The coupling capacitance is the part of the circuit that will set the coupling to the outside world, the amount of signal that can leave the resonator. Therefore the coupling capacitance sets the external Q value. To be visible in reflection measurements the coupling cannot be too low but in order to ensure remaining information inside the resonator it cannot be too strong either. Preferably the coupling is close to critical, $Q_{int} \approx Q_{ext}$. Using an estimated internal Q, a value for the coupling capacitance can be calculated. Capacitors can be simulated in Microwave office but also modeled numerically by conformal mapping [26]. In this way a capacitance value and corresponding design can be chosen. In these measurements an interdigitated capacitance has been used. According to simulations in Microwave office it has a capacitance of around 30 fF. A picture of the coupling capacitance used can be seen in Fig. 3.2.

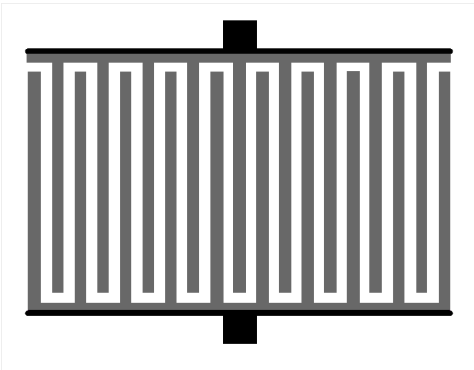

Figure 3.2: A model of the coupling capacitance structure used in this project, the fingers are $44\,\mu$m long, $2\,\mu$m wide and the separation of fingers are $2\,\mu$m.

To tune the SQUIDs independently, on-chip tuning lines are used. A current, I is applied to a transmission line passing close to the SQUID and terminated further away in the groundplane. This creates a magnetic field around the conductor. In turn this magnetic field creates a flux in the SQUID loop, tuning the cavity resonance frequency. Following the Biot-Savart law [27], the flux in one SQUID can be calculated as

$$\Phi = \frac{2\mu_0}{4\pi} \frac{I}{d} A,$$

where d is the distance between the tuning line and SQUID loop and A is the loop area. This is a rough estimation including the assumptions that the magnetic field

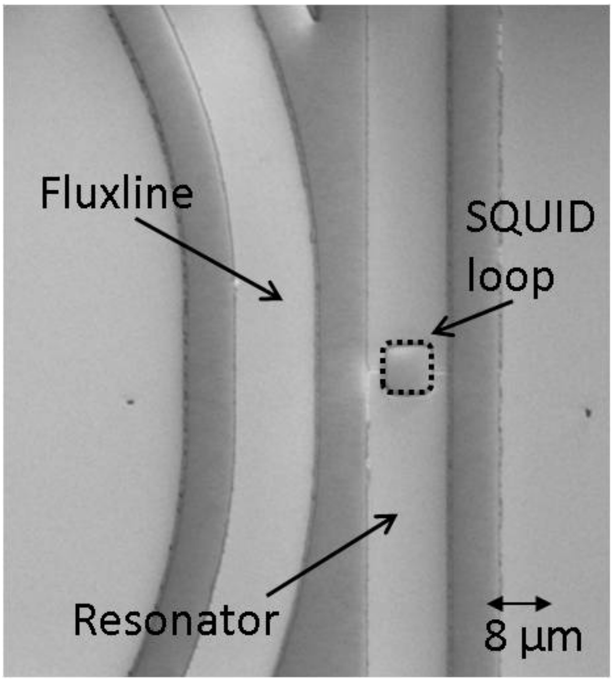

Figure 3.3: A SEM (scanning electron microscope) picture of a SQUID with corresponding fluxline. The SQUID loop is marked with black dashes.

is homogeneous over the SQUID loop and that the tuning line is a long and straight conductor. It can be seen in Fig. 3.3 that this is almost the case. In this figure the final tuning line design is depicted. To avoid currents flowing in the chip groundplane they are led off chip and grounded on the sampleholder. Other tuning line models tried in this project are shown in Fig. 3.4. When grounding in the aluminum groundplane currents were allowed to flow freely in the groundplane and through the resonator which created a strong crosstalk between the SQUIDs. One attempt to cut the flowing currents consisted in adding a gap in the middle of the resonator, small enough to let the microwave signals pass but cutting DC current. However it resulted in an avoided level crossing indicating a division into two coupled resonators, see appendix B and this solution was abandoned.

3.3 Circuit Layout

After modeling and simulating to decide dimensions on the different components, an AutoCAD drawing is made to use for electron beam lithography, *i.e.* defining the circuit on the chip. To have a chip compatible to the sample holders the structure needs to be patterned on a 5 by 5 mm chip and the contact pads need to be placed to allow for electrical connection of the chip in the sample box. In Fig. 3.5 a full chip drawing can be seen: in orange the structures that need the most precision like SQUIDs and

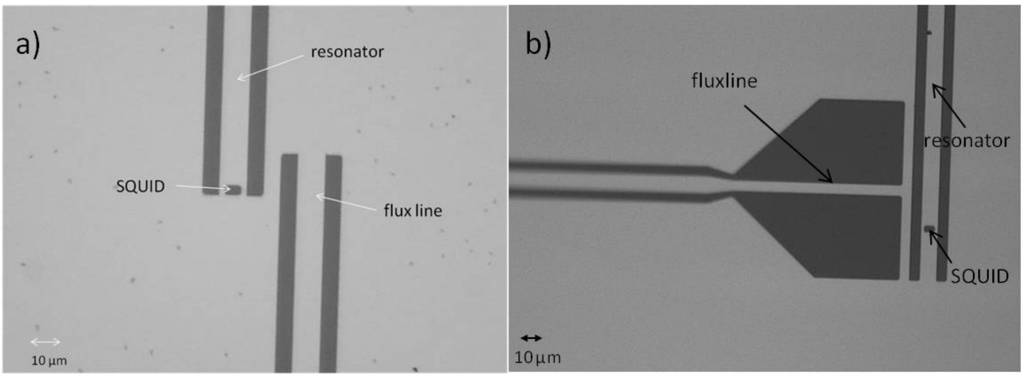

Figure 3.4: Microscope pictures of rejected fluxline designs. a) This design brought poor tunability, one reason because the current flowing out in the groundplane is splitting up and a part of it can flow down between the fluxline and the resonator creating a magnetic field in the opposite direction compared to the one from the fluxline, implying that the resulting flux in the SQUID loop becomes very small. b) To avoid these competing magnetic fields a design was chosen were the current flow was forced in one direction resulting in a visible tunability though currents are in this design also allowed to flow around in the chip groundplane.

capacitors and in green the resonator, fluxlines and groundplanes. All orange and green structures are made in aluminum and defined by electron beam lithography. Blue is the larger chip structures that are done in gold with photolithography. Because it is hard to fit a 12 mm long resonator on a small chip in full length the resonator is made in a meander shape which do not affect the functionality. Other things to take into account when designing is that transmission lines should not be placed too close to each other to prevent unwanted coupling and resonance effects. In Fig. 3.6 a microscope picture of a fabricated chip can be seen together with SEM (scanning electron microscope) zoom ins on one of the SQUIDs and the coupling capacitance. On the sides of the chip, test structures can be seen that include SQUIDs identical to the two in the resonator ends.

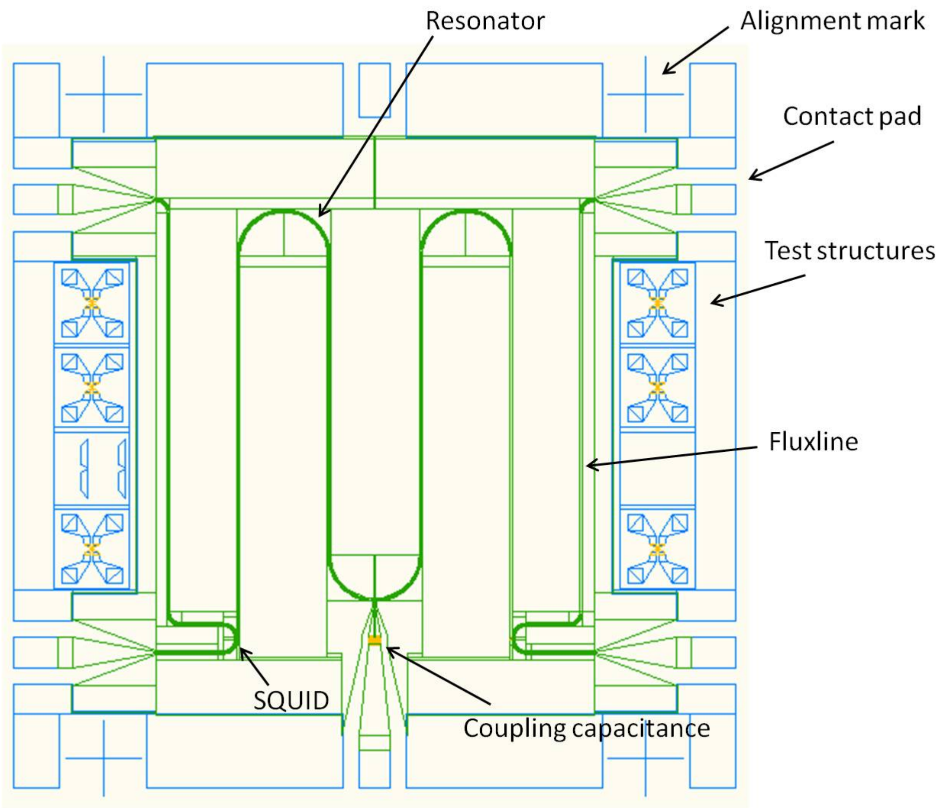

Figure 3.5: The CAD drawing of the chip with circuitry. Green defines the aluminum structures as resonator, tuning lines and groundplane. Orange are SQUIDs and the coupling capacitance, the smallest details that need higher precision. Unfortunately the SQUIDs in the resonator ends are too small to be visible in this drawing. The blue color represents the contact pads, alignment marks and some more groundplane.

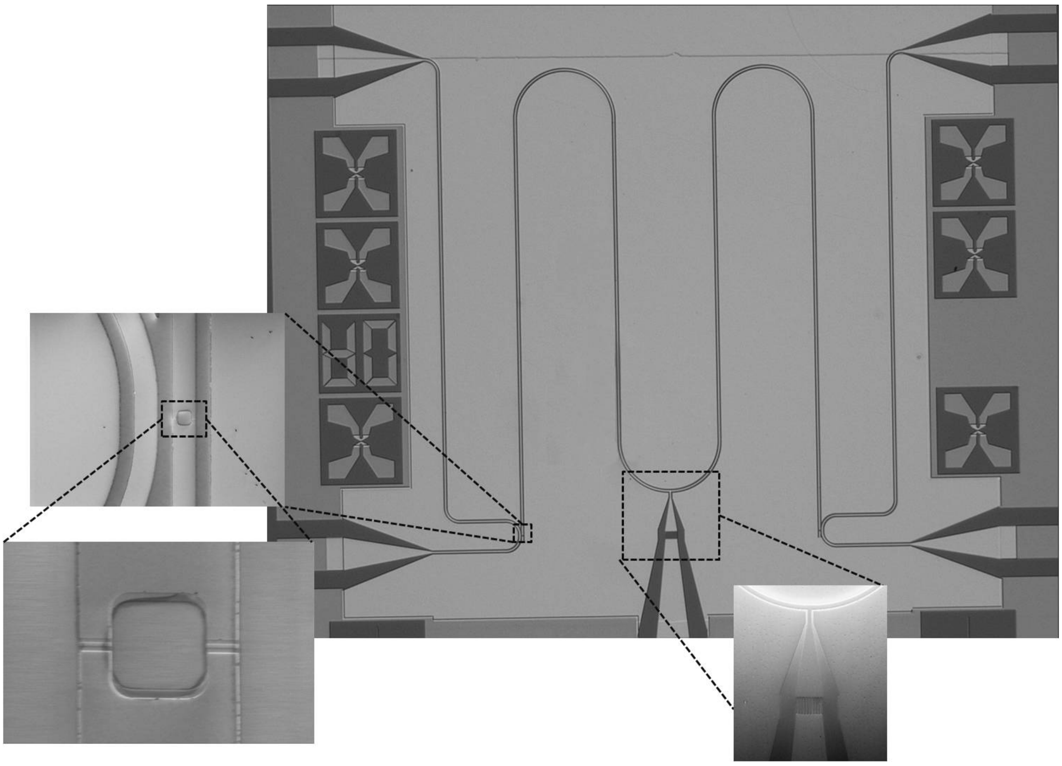

Figure 3.6: A finished fabricated chip. In the zoom in on the right the interdigitated coupling capacitance can be seen. On the left a zoom in on first the SQUID and corresponding fluxline and then on the SQUID itself.

4

Fabrication

The samples are fabricated on silicon substrates in the following procedure (a recipe can be found in appendix A); First photolithography is used to create the larger structures such as contact pads and alignment marks, Fig. 4.1. The contact pads are made from gold, because gold does not oxidize which ensures good contact in measurements later on. It has also the advantage of being non-magnetic. A polymer-based photoresist is spun on the wafer and then it is exposed to UV-light through a mask defining the pattern. The light breaks the polymer chains, and after exposure, when putting the wafer in a developer, the exposed polymer is dissolved and removed. Then the gold is deposited by an evaporation process. To remove unwanted gold, the sample is once more put in a solvent to lift-off the remaining resist.

To save time many identical chips are produced on wafers in the first step, the photolithography and gold deposition. Thereafter the wafer is semi-diced, *i.e.* diced from the backside halfway through. It leaves a wafer strong enough to go through the e-beam lithography process.

In the e-beam all the aluminum structures are defined, such as the resonator, SQUIDs, coupling capacitor and groundplane. Similarly to the photolithography process the wafer is covered with resist but in this case the writing is not done with photons but with electrons. Instead of an optical mask a CAD drawing is used to define the pattern. Because the substrate is bombarded with electrons it tends to be charged and electrons are scattered which gives a proximity effect to account for.

After development of the e-beam resist it is time for evaporation of aluminum. This is done in two steps with two different angles with an oxidization in between to create the tunnel barrier. This is called two-angle evaporation and in Fig. 4.2 the procedure is described. An advantage of this method is that the full junction can be fabricated in one process were the oxidation can be controlled and only one lithography step is needed.

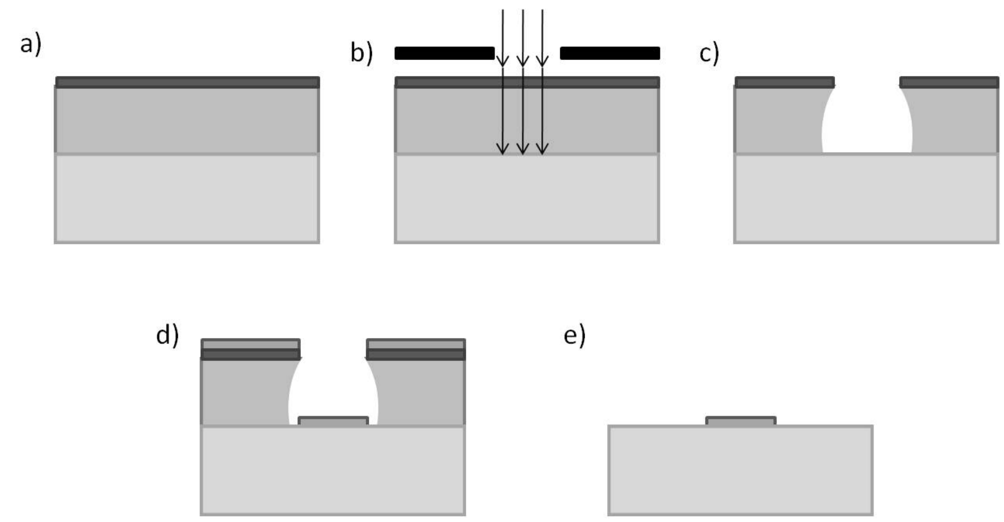

Figure 4.1: Step by step illustration of the photolithography lift-off process. a) A substrate with two layers of resist. Two layers are used to get an undercut. b) Photolithography. Defining the pattern in the resist by shining UV-light through a mask. c) The pattern is obtained by developing in a suitable chemical. While there is two layers of resist an undercut is formed. d) Evaporation of metal. Following the pattern, the structures are formed on the substrate and conveniently thanks to the undercut, no metal is sticking to the resist wall. e) Lift-off. The remaining resist and metal are removed from the substrate.

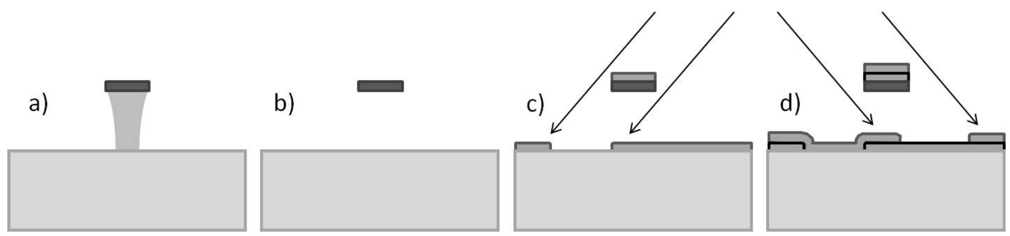

Figure 4.2: Two angle evaporation, to fabricate junctions. a) After e-beam lithography, the resist is developed. b) A two layer resist is used to get an undercut, that in this case when having a thin structure forms a suspended bridge also called Dolan bridge that defines the junction. c) The evaporation of metal is directional, evaporating towards the bridge with an angle causes a gap in the aluminum layer. d) After evaporation in the first angle, the metal is left oxidizing and then in a second angle another layer is evaporated, forming a SIS (superconducting-insulating-superconducting) junction in the middle, beneath the resist bridge.

5

Measurements

To measure on superconducting structures, they have to be cooled to a temperature lower than the materials critical temperature. In the case of thin film aluminum this means a temperature lower than 1.4 K. This is done in high technological fridges called cryostats. A cryostat is cooled using liquid nitrogen or helium, depending on the required temperature. The liquid nitrogen boiling point is at 77 K while liquid helium has a boiling point of 4.2 K, which makes them useful in different temperature ranges. For low temperature superconductors such as niobium and aluminum helium is used.

5.1 Cryogenics

Liquid helium (He^4) has a boiling temperature of 4.2 K but the critical temperature of aluminum is 1.4 K. To take the cryostat further down in temperature a mixture of He^4 and He^3 is used. When reaching temperatures of less than 0.8 K, which can be done by pumping on the liquid, a phase separation occurs in the mixture. Then pumping on the mixture removes light He^3 atoms and the equilibrium is disturbed. To reinstall equilibrium He^3 atoms need to cross a phase boundary, which costs energy. The energy is found in form of heat and the phase transition absorbs heat and cools the system. This is the working principle of a dilution refrigerator.

A cryostat cools in different steps. In Fig. 5.1 a picture of the cryostat is shown. At the top is the flange where the Inner Vacuum Chamber (IVC) is sealed. Everything below the flange is kept under vacuum when the fridge is cold. The IVC is put in a liquid helium bath which gives a temperature of 4.2 K. Inside the IVC it is important to avoid thermal contact between circuitry and the IVC, to prevent heating. The first cooling level is the 1 K pot where the temperature is around 1.5 K reached by pumping on He^4. Next is the still where the He^3 atoms are pumped out and the temperature is around 600 mK. Through heat exchangers the mixture reaches the mixing chamber

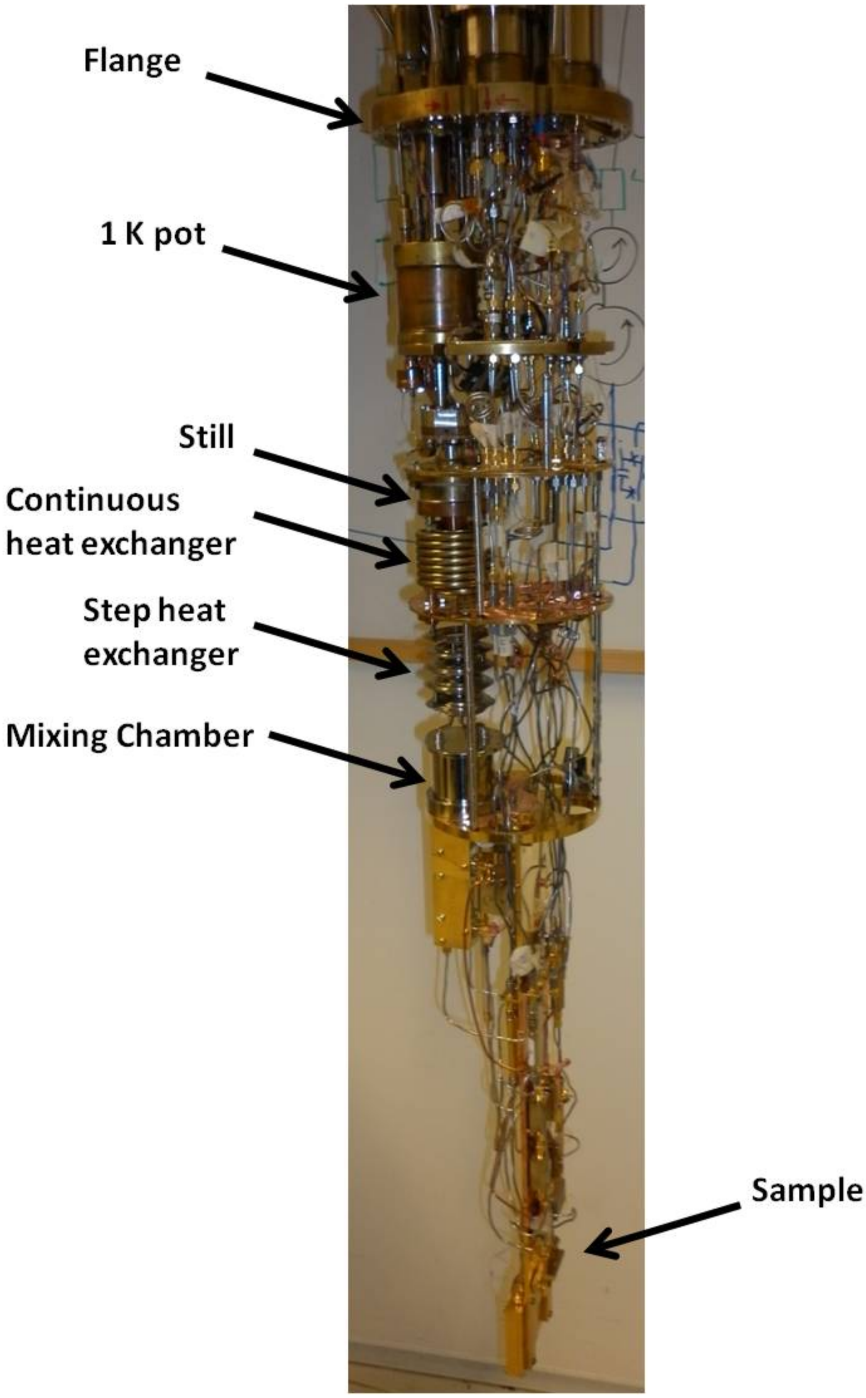

Figure 5.1: A picture of the interior of the cryostat, all the cooling steps. At the bottom of this stick is where the sample is placed on the tail in good thermal contact with the mixing chamber which is the coldest part of the fridge.

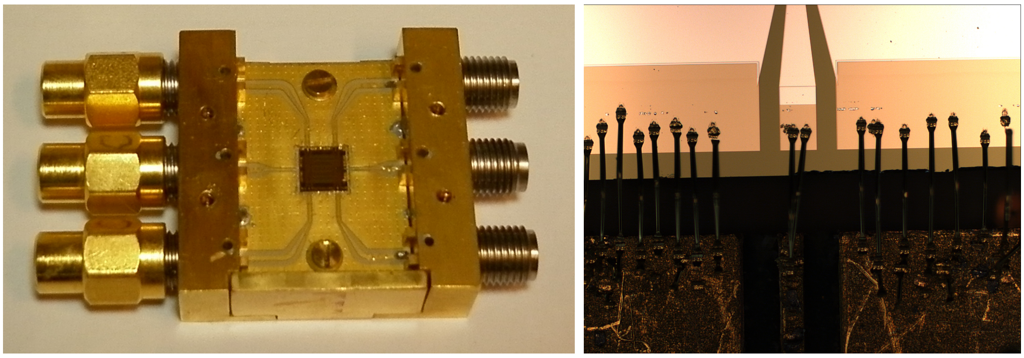

Figure 5.2: On the left the samplebox with the glued and bonded chip can be seen and on the right a zoom in on some of the gold wire bonds connecting the chip to the circuit board of the box.

which is the coldest part where temperatures lower than 30 mK can be reached. This is where the sample is placed on a copper tail that is in good thermal contact with the mixing chamber. The chip is glued to a sampleholder and the electrical connection is established by bonding with gold wire, Fig. 5.2.

5.2 Measurement

When measuring in a cryostat it is important to have good electrical and bad thermal conductivity between different temperature stages. Ideally superconducting cables are used to avoid heat transport though they can only be used at the lower levels were the temperature is lower than the materials critical temperature. From the still and up stainless steel coaxial cables are used, because stainless steel has bad thermal conduction. In the other direction, from the still to the mixing chamber the temperature is lower than 1 K, niobium cables are used, since they are superconducting at this temperature and superconductors do not conduct heat well. All high frequency cables as well as the transmission lines on the chip are matched with 50 Ω characteristic impedance in order to avoid reflections.

To prevent noise from traveling down in the cables, filters and attenuators are connected according to the schedule in Fig. 5.3. The attenuators reduce the power of the signal and contribute to the thermalization on each temperature level in the cryostat. Low pass filters and powder filters are used to exclude noise and high frequency radiation. The marked capacitance-inductance part indicates two bias-tees, in which AC and DC signals are combined. In this setup one cold amplifier was included (LNA) but also two room temperature amplifiers were used. In addition some extra room-temperature attenuation was added. To prevent noise reflection back to the chip, a circulator is used that works like a roundabout were the signal only can travel in one direction. Back reflected signals are sent to a 50 Ω terminator resistance. To further expel noise from the outside world a magnetic shield is attached beneath the still level. This shield cuts

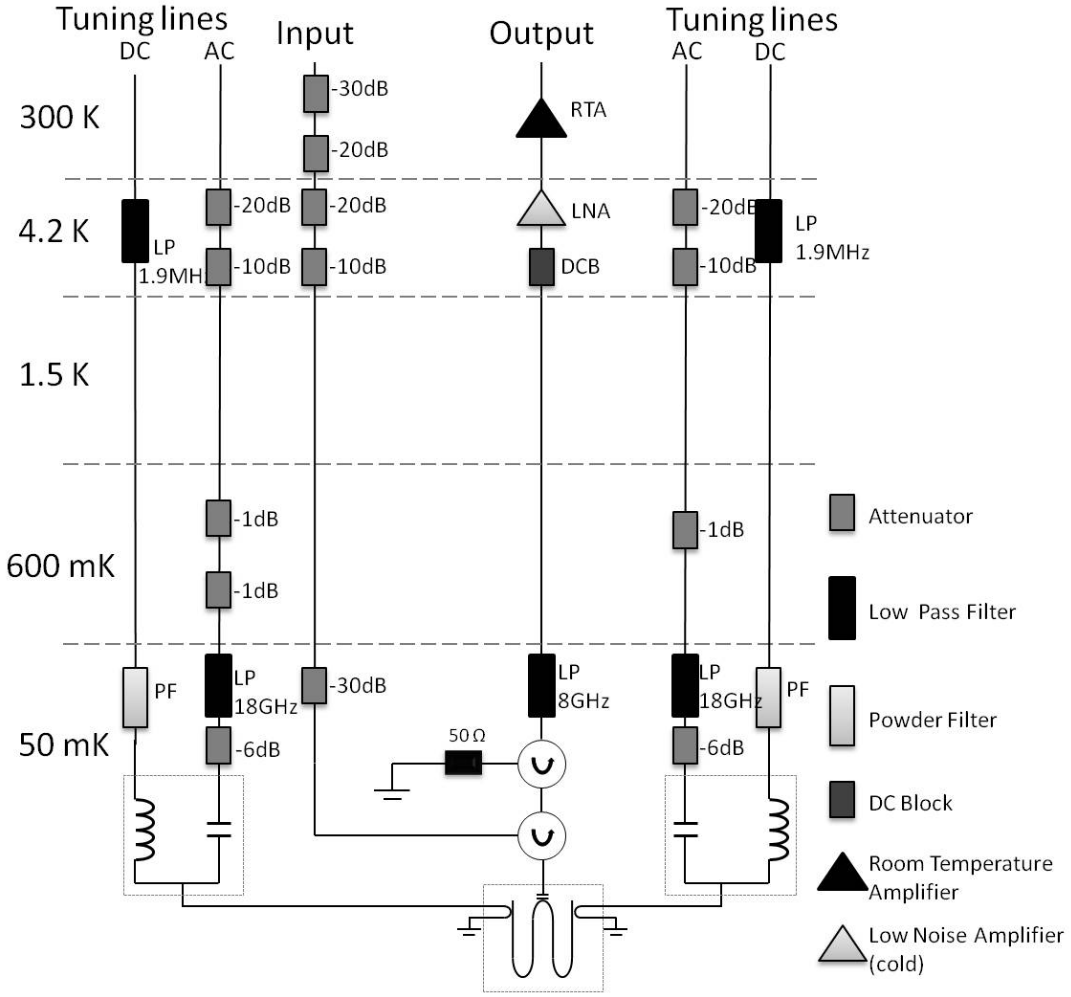

Figure 5.3: The setup used in the dilution refrigerator to filter noise and thermalize cables. At the bottom of the schematic the chip is drawn.

radiation but also magnetic fields. Since the magnetic fields created by the fluxlines are very small the shielding of magnetic fields from other sources is important to keep the noise levels lower than the measurement signal levels. Fig. 5.4 shows a picture of the setup on the copper tail, the circulators, bias tees, and the sample box.

The resonator characterization and SQUID DC tuning measurements are done with a Vector Network Analyzer (VNA). With the VNA both reflection and transmission measurements can be done. The signal sent down from room-temperature needs to be thermalized and filtered while the signal reflected back from the chip needs to be amplified to be visible. Hence it is convenient to use a circulator and create a "fake" reflection measurement. From the chip point of view, reflection (S_{11}) is measured, a signal is sent in and the signal reflected back is measured. Whereas on the VNA, S_{21} is

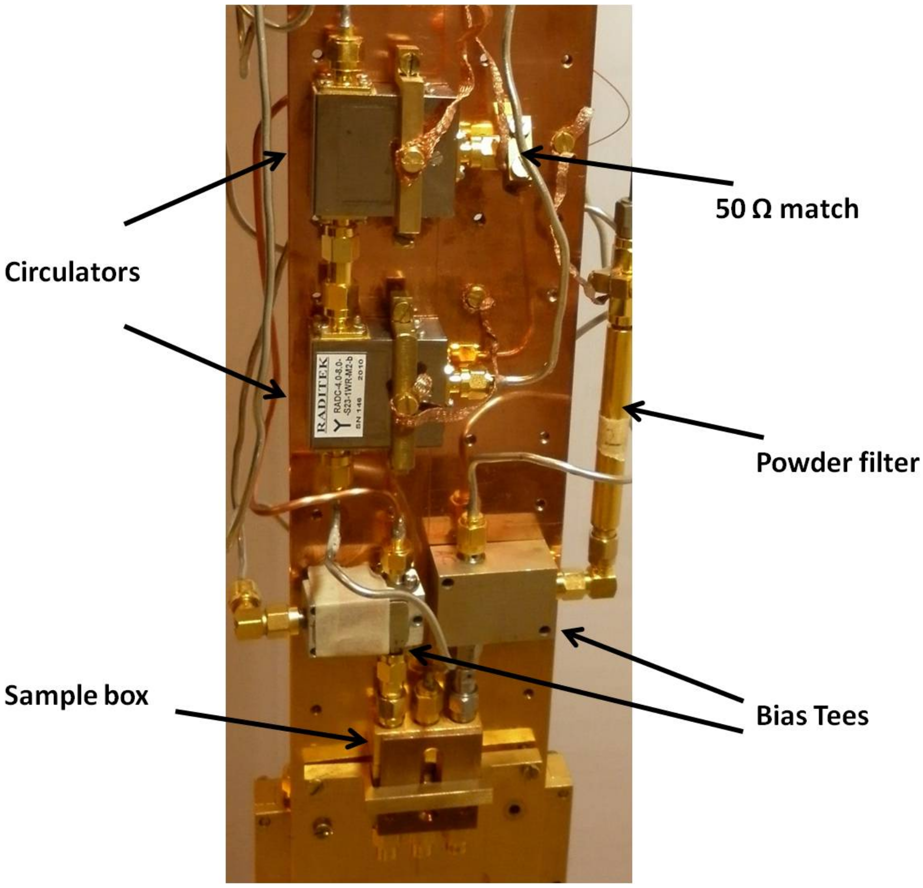

Figure 5.4: The setup as it was mounted on the tail. To be compared to the schematic of the setup.

measured, a signal is sent in and due to the circulator the reflected signal travels through a different path back to room temperature. Using scattering matrix formulation

$$\begin{pmatrix} \Gamma_1^- \\ \Gamma_2^- \end{pmatrix} = \begin{pmatrix} S_{11} & S_{12} \\ S_{21} & S_{22} \end{pmatrix} \begin{pmatrix} \Gamma_1^+ \\ \Gamma_2^+ \end{pmatrix}.$$

Γ_n^- denotes the reflected signal from port n and Γ_n^+ the incoming signal corresponding to the same port ($n \in$ 1,2). For resonators in general the reflection coefficient S_{11} can be written as in (2.12).

6

Results

With test measurements in a He^3 cryostat, where only temperatures of around 300 mK can be reached, a design was developed with a suitable coupling and tunable resonance frequency. The results presented here are measured with a chip of the type shown in Fig. 3.6 in a dilution refrigerator. In order to measure photon generation caused by parametric effects, the system first has to be characterized with DC flux tuning and then with high frequency modulation of the boundary conditions. Finally photon generation has been measured as afunction of phase offset between the two oscillating mirrors. Two cases have been treated, one driving the modulation at two times the resonance freqeuncy and a driving of three times the resonance frequency, as discussed in the introduction.

A stable base temperature of around 50 mK in the cryostat was used. Resistance measurements[1] of the SQUID test structures gave a normal resistance $R_N = 196\,\Omega$, which corresponds to a critical current of $I_c = 1.7\,\mu$A. This critical current corresponds to a Josephson energy $E_J = 41\,$K. The resonator length was 11.94 mm.

When working with fluxes, there is a risk of trapping flux in the SQUID loops. Trapped fluxes cause offsets in DC flux tuning and has to be compensated for. The difficult part with these offsets is that they are not constant. If the system for some reason is heated or disturbed by a strong signal, or for no obvious reason at all, this trapped flux can be released and cause a fluxjump, *i.e.* a change of the DC flux offsets. In all the measurements these offsets have been taken into account and compensated for.

6.1 Resonator Characterization

To characterize the resonator a signal is applied to the probe line and magnitude and phase of the reflection coefficient is measured. The frequency of the input signal is swept

[1] Four point resistance measurement was used.

over an interval and at the resonance frequency a part of the incoming power is absorbed by the resonator. These measurements are done with zero flux applied to the SQUID loops. Fig. 6.1 presents the result, the first graph shows the magnitude of the reflection coefficient and the second the phase. On the right, the phase and magnitude signals are combined in a polar diagram. The dots represent measurement data and the curves a fit. It can be noted that the magnitude signal has been normalized to have a background equal to one.

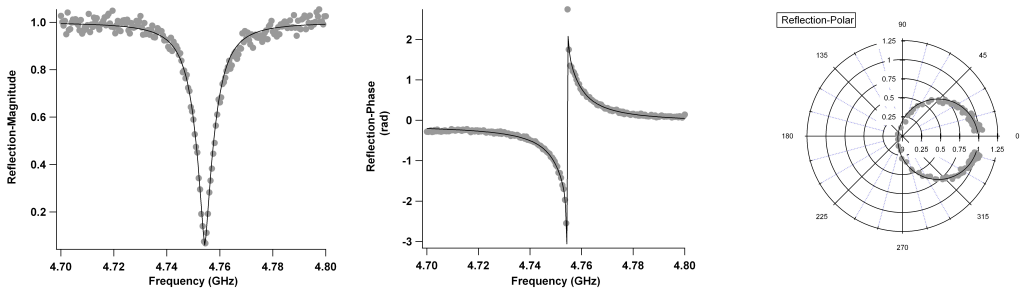

Figure 6.1: Reflection measurements of the resonator in its ground state. On the left the normalized magnitude signal and in the middle the phase signal. On the right the magnitude and phase signals are combined in a polar plot. The dots correspond to data and the lines to fits.

The polar plot shows that the resonator is (just barely) overcoupled, which implies that the internal quality factor is larger than the external. It can be seen on the polar plot which makes a loop around the origin, and from the 2π phase shift in the phase signal. Since tuning of the SQUIDs induce internal losses in the resonator, *i.e.* decreased Q_{int}, it is convenient to be overcoupled in the unmodulated state to ensure visibility of the signal.

This data has been fitted to the model (2.12) to extract the resonator characteristics,

$$\Gamma = \frac{\frac{1}{Q_{ext}} - \frac{1}{Q_{int}} - 2i\frac{\Delta\omega}{\omega_r}}{\frac{1}{Q_{ext}} + \frac{1}{Q_{int}} + 2i\frac{\Delta\omega}{\omega_r}},$$

with Q_{int}, Q_{ext}, ω_r and a phase offset as free parameters. Q-values for the fit presented in the figure are extracted as $Q_{int} = 858$, $Q_{ext} = 762$, which corresponds to a total Q-value of 404 using (2.6). The resonance frequency corresponding to the center point of the magnitude dip is 4.752 GHz. It can be noticed that compared to previous measurements on tunable cavities this Q-value is quite low [10, 11].

These characterization measurements have been done at a power on the input line of -5 dBm, which when subtracting the attenuation on the input line corresponds to -115 dBm at the sample. Taking several of these magnitude and phase traces for different probe signal power shows that at higher power the resonance frequency is shifted to lower frequencies, Fig. 6.2. On the left the magnitude signal is presented in the color scale, the green line in the middle corresponds to the resonance frequency and the blue is the

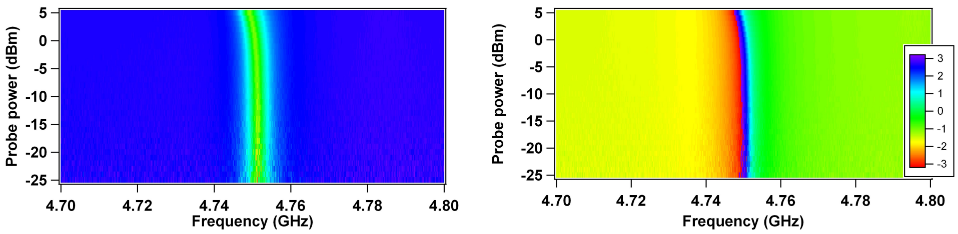

Figure 6.2: A reflection measurement of the resonator, the frequency spectrum has been probed as a function of power. On the left the magnitude of the reflection can be seen. The green dip in the middle corresponds to the resonance frequency. On the right the reflection phase signal is presented and the 2π phase shift can be seen in the color scale.

background where all signal is reflected back and nothing is transmitted into the cavity. The graph on the right in Fig. 6.2 presents the phase signal with the 2π phase shift visible as a color shift in the middle of the traces. This resonance shift is due to non-linear effects arising from higher currents flowing through the SQUIDs. Preferably the measurements are done in the linear regime, in this case below $-2\,\mathrm{dBm}$, which means that $-5\,\mathrm{dBm}$ is a suitable probe power to use.

6.2 DC Tuning

Using the same type of reflection measurement as for the calibration of the resonator, tuning of the resonance frequency can be performed. By applying a DC current to one of the DC tuning lines, the other one held at zero, a flux is applied to the SQUID and the resonance frequency is reduced, Fig. 6.3. The graph on the left shows the

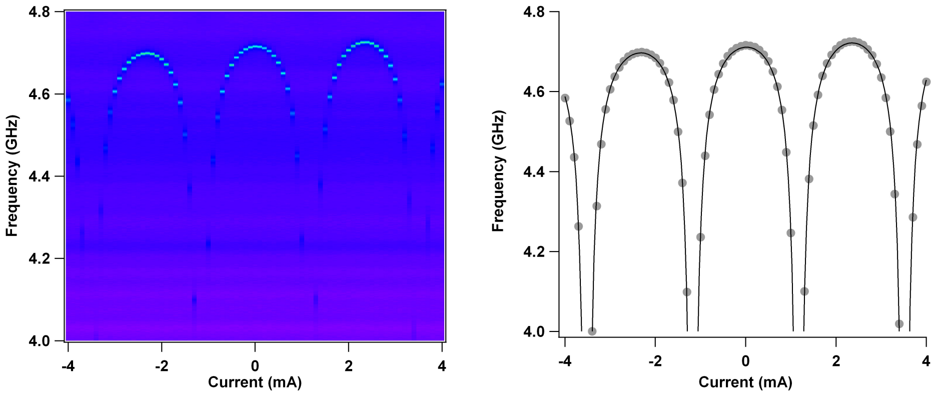

Figure 6.3: DC tuning of one SQUID. On the left the magnitude signal is presented and on the right the extracted resonance frequency as dots and a fit as a curve.

magnitude part of the reflection. The bright points represent the resonance frequency which is modulated by the applied current. On the right an extraction of the resonance frequency can be seen and also a fit to equation (2.14),

$$\omega = \frac{f_0}{1 + \frac{L_s^l}{L_l l} + \frac{L_s^r}{L_l l}}.$$

Since current and flux are linearly proportional to each other according to Biot-Savart law, the applied flux to the SQUID can be expressed in terms of the current applied to the tuning line as $\Phi = \alpha I$, where α is a proportionality constant that can be calculated. The SQUID inductance, (2.5) can be expressed

$$L_s = \frac{L_{s0}}{|\cos\frac{\pi\Phi}{\Phi_0}|}$$

and if rewriting Φ as the corresponding current and Φ_0 as the current corresponding to one flux quanta it can be expressed for one of the SQUIDs as

$$L_s^l = \frac{L_{s0}}{|\cos\frac{\pi(I_l + c_t \cdot I_r)}{I_0}|},$$

where I_l is the current applied to the tuning line in focus and I_0 is the amount of current corresponding to a flux quanta. To get a good fit a small crosstalk between the SQUIDs has to be assumed, since a small flux can escape from one tuning line and affect the opposite SQUID. Therefore I_r, the current applied to the second tuning line scaled by a factor c_t, is introduced. Hence for this experiment the bare frequency can be extracted as $f_0 = 5.08\,\mathrm{GHz}$, $L_{s0}/L_l l = 3.5 \cdot 10^{-2}$ and the crosstalk between the SQUIDs as 3.1 %. The current period can be deduced to 2.34 mA, which corresponds to one flux quanta. This gives an $\alpha = 8.85 \cdot 10^{-13}\,\mathrm{H}$. Note that in this fit the same parameters are assumed for both SQUIDs.

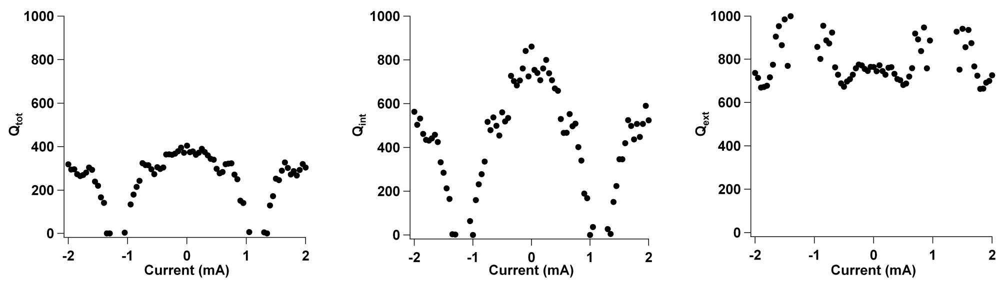

Figure 6.4: The Q values as functions of applied flux (current) for the DC tuning of one SQUID while the other one is held at zero flux. Total, internal and external Q values are presented.

In the color scale of the magnitude signal in Fig. 6.3 it can be seen that at larger detuning, the resonance dip is wider: it grows broader and less deep, indicating a decreased Q-value. Using the model from the characterization, the total Q can be extracted as a function of detuning, Fig. 6.4. In the middle graph where the internal Q-value is presented it can be seen that Q_{int} is decreasing when the detuning of the resonance frequency is increasing, an indication that the SQUID induces losses. The external Q-value is more stable and shows a small increase when the frequency is far detuned. An increase in external Q at lower frequencies can be explained by the coupling capacitance, which does not allow low frequency signals to pass (see equation (2.10b)). This implies a very weak coupling and at low frequencies read out of the cavity is no longer possible.

So far, tuning of only one SQUID has been considered. If sweeping the DC flux applied to both SQUIDs, the resonance frequency for each point can be extracted and shown as a function of the two fluxes (currents), which is done in the graph on the left in Fig. 6.5. In this figure the crosstalk between the SQUIDs is indicated by the slightly tilted structure. Compared to measurements including other tuning line designs as the one on the right, this crosstalk is very small. As showed above in Fig. 6.3 the tuning of the resonance frequency can be modeled and this two dimensional measurement can be fitted with the same values.

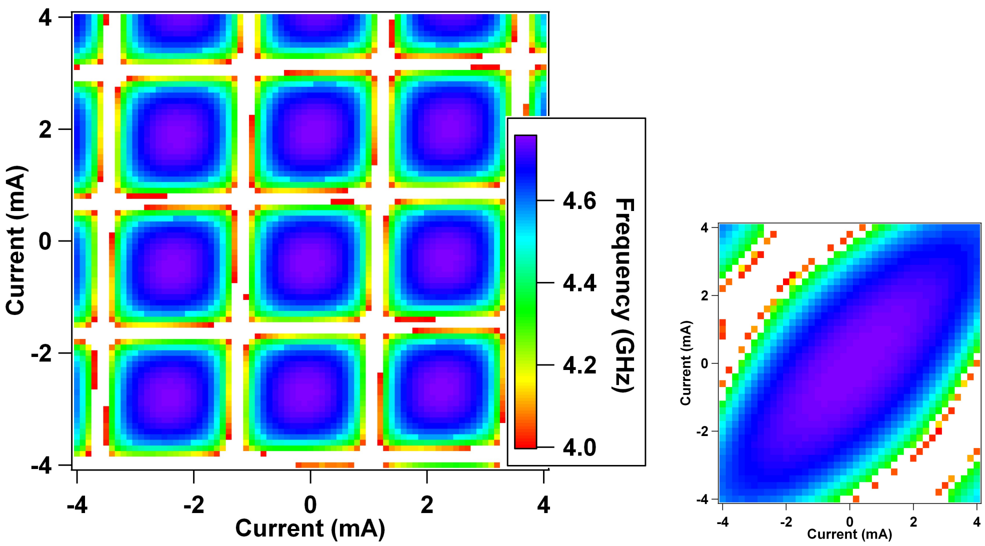

Figure 6.5: On the left: In color scale the resonance frequency is shown as a function of the fluxes applied on the two SQUIDs, x- and y-axis. It can be seen that the resonance frequency can be tuned by more than 700 MHz. On the right: The resonance frequency as a function of fluxes on the two SQUIDs with an early fluxline design (Fig. 3.4b) indicating a much higher crosstalk than the final, compare to Fig. 6.5.

6.3 Photon Generation

Photon generation in the cavity is attained by high frequency flux modulation of the SQUIDs [11]. Microwave signals are applied to the tuning lines in order to modulate the resonator boundary conditions. A DC bias point is chosen with the help of Fig. 6.3

and 6.5. At the bias point, the slope of the frequency modulation curve should be non-zero. With AC modulation of the SQUIDs, there are more parameters that can be controlled such as pump power and pump frequency for each SQUID. In the measurements presented here, the SQUIDs are always driven at the same frequency, which gives a phase offset as an additional parameter.

6.3.1 Single-Sided Modulation

The first attempt to generate photons is done by modulating only one SQUID. A drive power versus drive frequency measurement has been done, positioning the system at a bias point on a slope, where one SQUID is biased at zero flux and the other tuned to a DC flux of $-0.30\Phi_0$ (corresponding to a DC current applied to the fluxline of $-0.7\,\mathrm{mA}$). The drive power at the microwave generator is in this case expressed in amplitude, A_p which corresponds to a power of $20\log A_p$ in dBm. In this measurement, in contrast to the ones of the spectra, no signal is applied to the input line of the resonator. Fig. 6.6 shows the result, there is some radiation coming out. This signal is measured in a given bandwidth around half the frequency at which the resonator is driven. The small picture on the right indicates the bias point and pump direction.

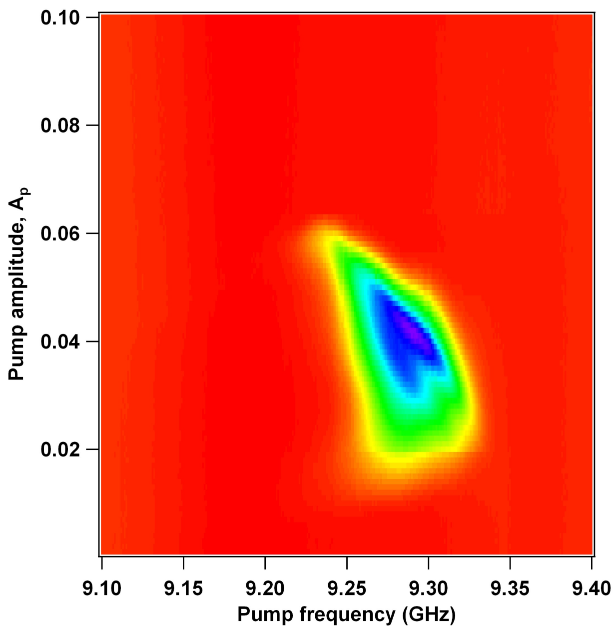

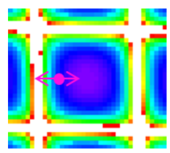

Figure 6.6: The color scale shows the radiation measured when driving one SQUID at a bias point, indicated in the small picture on the right, without applying any signal to the input line. Radiation is shown as a function of amplitude on drive power and the mirror oscillation frequency.

According to the theory of the parametric oscillator [21], at a threshold an exponential growth in time should be seen above some threshold pump amplitude. However these measurements presented are in terms of frequency. A sharp threshold can be seen, however the radiation is disappearing when the pump amplitude is increased further. This might be due to higher order non-linearities in the system.

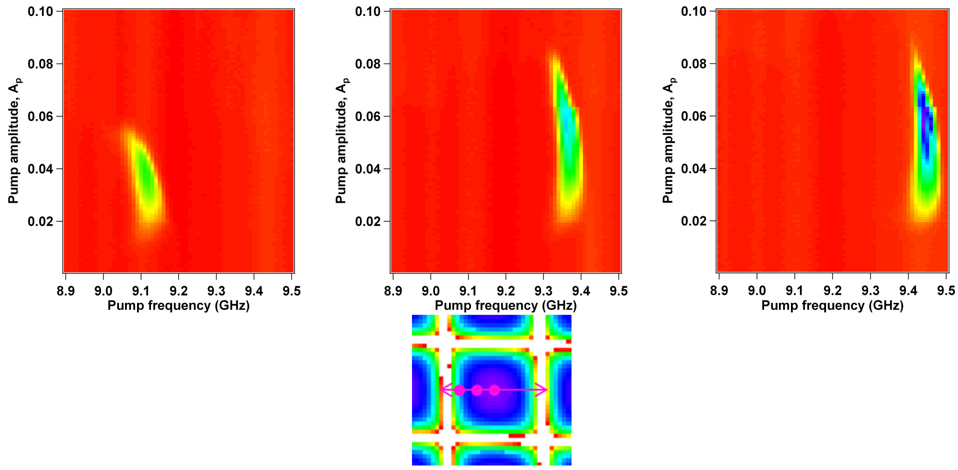

Figure 6.7: The three graphs are measuring radiation coming out from the cavity at different bias points, indicated by the bottom picture. The graph on the left represents the bias point furthest down on the slope and the one on the right corresponds to zero flux, the top of the hill, and the middle one corresponds to the middle bias point.

The amount of radiation generated and the location of the generation in the frequency-power plane should be bias point dependent. Fig. 6.7 shows three graphs for three different bias points, one from down on the slope $\Phi_{DC} = 0.34\Phi_0$, one a little bit higher at $\Phi_{DC} = 0.21\Phi_0$ and one at the top (zero flux). The small DC tuning picture shows the bias points and modulation direction. A closer look gives that the pump frequency required for generation of radiation follows twice the resonance frequency of the bias point, which is expected. Regarding the pump power required for photon generation, no clear bias point dependence can be seen. Naively one would expect a lower power needed for creating a visible modulation when biasing on a steeper slope. However this is not the case, also the Q value plays a role. As seen in Fig. 6.4 a higher detuning gives a lower Q value. A comparison between the graphs in Fig. 6.7 gives that the generation of photons is saturated at a lower power when the Q value is lower.

A complexity that has to be taken into account when analyzing the resonator behavior is interaction of higher modes. Compared to previous tunable cavity experiments this resonator is a $\lambda/2$ instead of $\lambda/4$ which means that when driving at twice the resonance frequency, 2ω, the driving frequency is equal to the second mode of the cavity. This means that when driving the field inside, the cavity can be excited before the parametric amplification threshold is reached and thereby the generation of photons visible is no longer solely due to excitations of vacuum fluctuations but down conversion of higher modes.

6.3.2 Calibration of Flux Coupling-The 2ω-case

To do a characterization of AC tuning line coupling of each SQUID, one side is modulated while the other one is held at a fixed flux. The frequency spectrum of the resonator is probed as a function of power on the signal applied to the tuning line while the drive frequency is constant at 8.92 GHz corresponding to two times the resonance frequency at the bias point. A symmetric bias point is chosen, *i.e.* to have the same amount of flux in both SQUIDs $\Phi^l_{dc} = \Phi^r_{dc} = 0.21\Phi_0$. The results are shown in Fig. 6.8 as diagrams of magnitude signals. As can be seen the resonance frequency at lower power is constant while for higher power it bends off and fades. The bend is due to non-linearities in the modulation and the disappearance might be due to increased losses in the system.

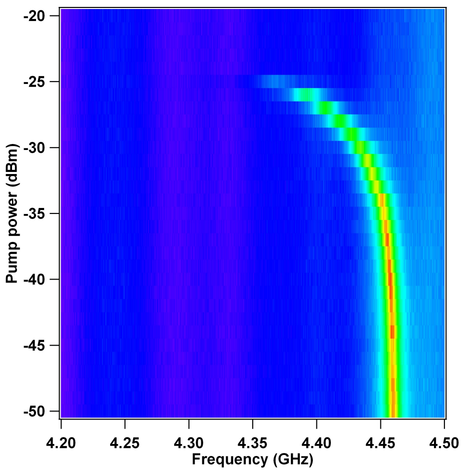

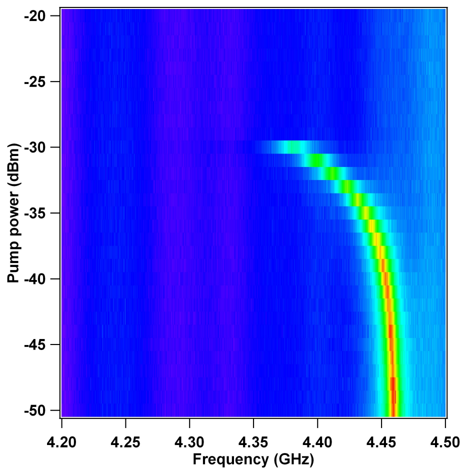

Figure 6.8: In the two graphs the frequency dependence as a function of pump power is displayed for the two SQUIDs separately. The magnitude signal from a reflection measurement is shown. This measurement has been done with a pump frequency of 8.92 GHz.

The right graph shows a shift at lower power compared to the left one. This can be due to a difference in attenuation for the two tuning lines, which is likely to happen because the lines differ in length. In addition the two tuning lines do not have exactly the same amount of added attenuation, as can be seen in the setup Fig. 5.3. A comparison between the two bends gives a calibration of the power offset that can be used when applying a signal to the tuning lines in order to drive both SQUIDs with the same flux amplitude.

Since the frequency bend corresponds to the fluxline-SQUID coupling it can be fitted as a first approximation with the same model as the static tuning curve (2.14). The total flux applied to the SQUID at a time t can be assumed to be

$$\Phi(t) = \Phi_{bias} + \Phi_{ac} \cos \omega_p t,$$

where Φ_{ac} is the flux amplitude of the pump signal and ω_p the drive frequency. For each power the frequency can be fitted by taking an integrated value over one period.

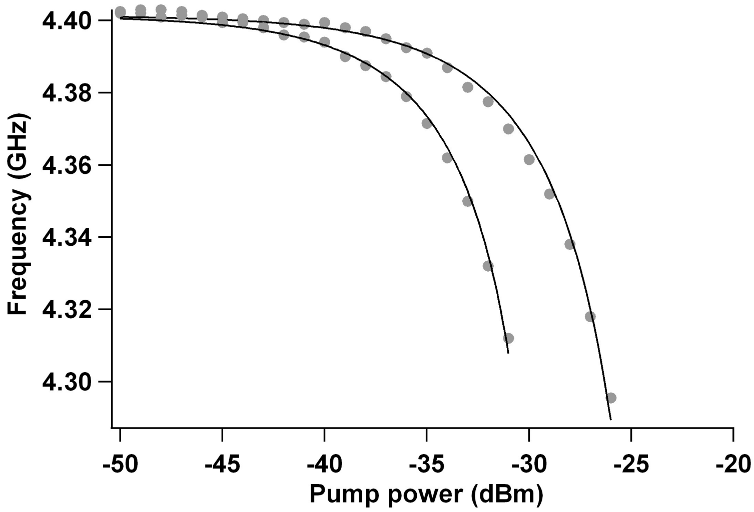

Figure 6.9: An extraction of the resonance frequency in Fig. 6.8, which have been fitted to a model in order to calculate the tuning line-SQUID coupling.

As before, the fluxes are rewritten as currents and Φ_{ac} as a function of the drive power. All parameters are assumed to be equal to the parameters extracted for the static case. The only free parameter is β defined by $I_{ac} = \beta 10^{\frac{P_p}{20}}$, where P_p is the pump power in dBm. The result can be found in Fig. 6.9, dots representing the data and the curve the fit. For the two SQUIDs β is extracted as 3.78 mA and 10.7 mA respectively. This provides a calibration of how the power applied to the tuning line relates to the flux in the SQUID. Hence this coupling parameter includes losses in coaxial cables, attenuators and the bias tee as well as on chip tuning line-SQUID loop coupling. Since the fluxlines are grounded the microwave signal forms standing waves, which gives also a frequency dependence to β. Instead of grounding, the fluxline could have been terminated by a $50\,\Omega$ impedance and the waves would have been propagating instead of standing.

6.3.3 Two Sided Modulation-The 2ω-case

Driving both SQUIDs simultaneously instead of one at a time, the phase difference between the two driving signals affect the outcome. An experimental difficulty is that each time the pump frequency is changed the phase is randomly set. This phase offset affects the photon generation while it determines how the boundary conditions are oscillating with respect to each other, as showed in Fig. 1.2. Probing how the frequency spectrum behaves as a function of phase offset is shown in Fig. 6.10, on the left for a pump power of -40 dBm and on the right -30 dBm, which when taking the attenuation on the lines into account corresponds to -77 dBm and 67 dBm. The calibration from Fig. 6.8 is used to apply the same power to both SQUIDs and the drive frequency is constant.The system is biased in a symmetric point, $\Phi^l_{dc} = \Phi^r_{dc} = -0.3\Phi_0$. As expected, the resonance frequency modulation is higher for higher power. If the frequency modulation was linear, no phase dependence of the resonance frequency would be seen. However the measurements are averages in time and a modulation appears as an effect of the non-linear pumping. In practice the non-linearity of the SQUIDs inductance $\cos \pi\Phi/\Phi_0$ causes a not perfectly sinusoidal movement of the "mirrors". The mirrors move further in one direction than in the other one from the bias point. It can be deduced that the maximum resonance frequency corresponds to the translational mode because this is when the mirrors move with a constant distance and the resonance frequency is constant. When the mirrors oscillate symmetrically around the center, the resonance frequency is changed over time and is where the non-linearity affects the time-averaged measurement. This corresponds to the lowest measured resonance frequency and the breathing mode.

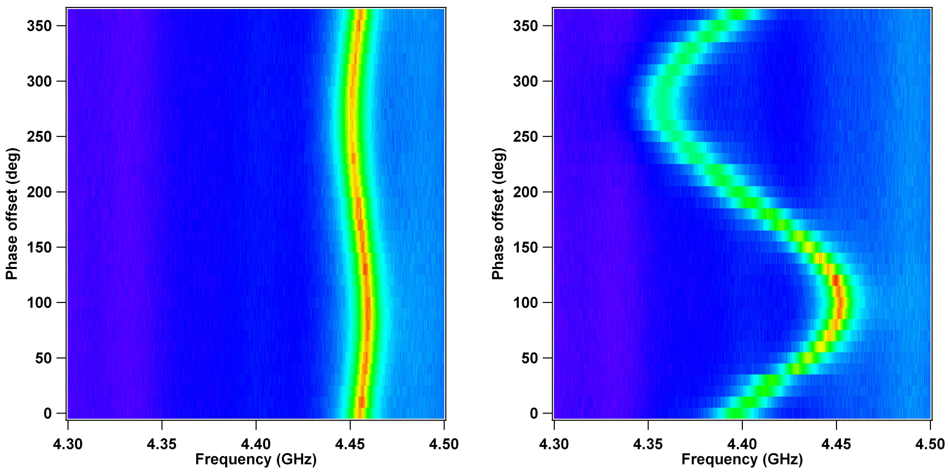

Figure 6.10: The frequency spectra is probed as a function of phase offset between the two pumps. On the left for a lower pump power and on the right for a higher.

For each pump frequency the generation of photons can be measured as a function of pump power and phase offset. Note that there is no signal applied to the input line. Repeating this for several pump frequencies, the generated radiation can be plotted as a function of pump power and frequency for different phase offsets. To find the phase corresponding to the breathing and translational modes for each drive frequency, a corresponding measurement similar to the one in Fig. 6.10 is done. In Fig. 6.11, the breathing and translational mode are presented and the measured power is normalized to the background. In agreement with theory, radiation is generated in the breathing mode but not in the translational mode [2]. However in these measurements a small output can be seen also in the translational mode for very high pump power, which may be explained by leakage from higher modes or a non-linear pumping curve.

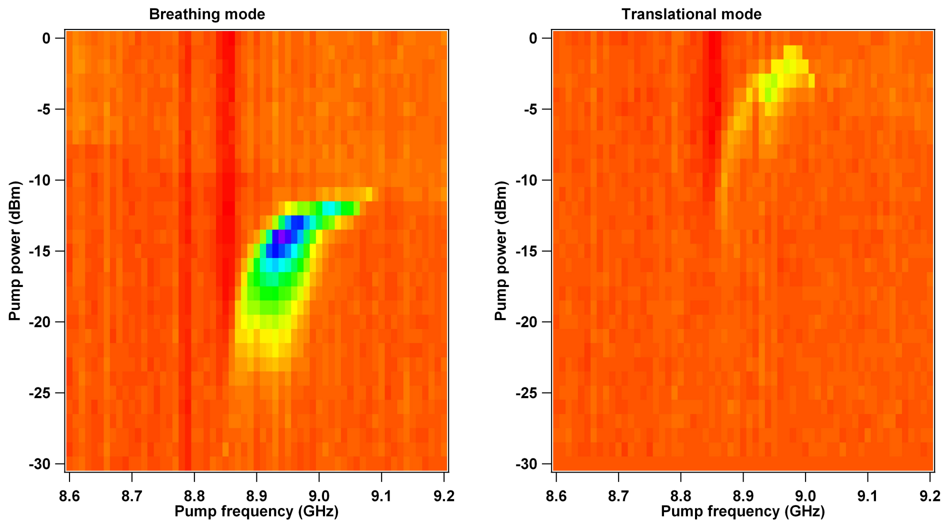

Figure 6.11: In the color scale the radiation coming out of the cavity as a function of pump power and pump frequency for driving around two times the resonance frequency. On the left the breathing mode and on the right the translational mode.

6.3.4 Calibration of Flux Coupling-The 3ω-case

Driving the two SQUIDs simultaneously can also be done at three times the resonance frequency, 3ω. In Fig. 6.12 a calibration measurement similar to the one for the 2ω-pumping can be seen. The resonance frequency is probed, sweeping the power of the

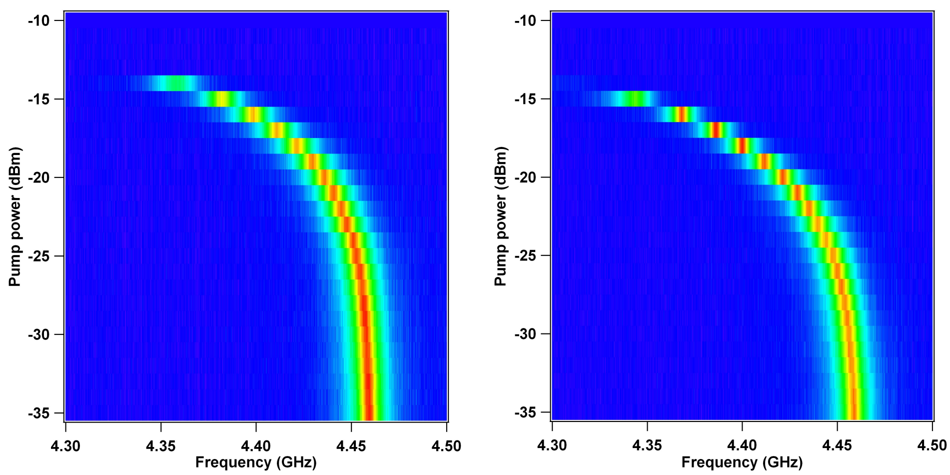

Figure 6.12: The graphs show how the resonance frequency is modulated as the pump power is increased for one SQUID at a time. Pump frequency is held at three times the resonance frequency of the bias point which here means a pump frequency of 13.38 GHz.

applied AC tuning signal. Here the SQUIDs are driven one at a time with a pump frequency of 13.38 GHz holding the other one constant at the bias point. A shift in the resonance frequency appear at higher power because of non-linearities in the system. Compared to the 2ω-case the applied power needed to induce non-linear effects to shift the resonance is higher. This can be due to a higher attenuation in the coaxial cables for higher frequencies. Though the difference in tuning line-SQUID coupling between the two lines is smaller at this higher drive frequency.

6.3.5 Two Sided Modulation-The 3ω-case

Fig. 6.13 shows the resonance spectrum for different phase offsets at a lower and higher pump power respectively. The same effects can be seen as in the 2ω-case, a higher power modulates the resonance frequency more due to the non-linear SQUID inductance. Remembering the space-time diagram in Fig. 1.2, it can be concluded that when pumping at three times the resonance frequency, the mode that does not change substantially in resonance frequency is the breathing mode. This implies that the highest resonance frequency corresponds to the breathing mode and the lowest to the translational mode. In contrast to the 2ω-case where the higher resonance frequency corresponds to the translational mode.

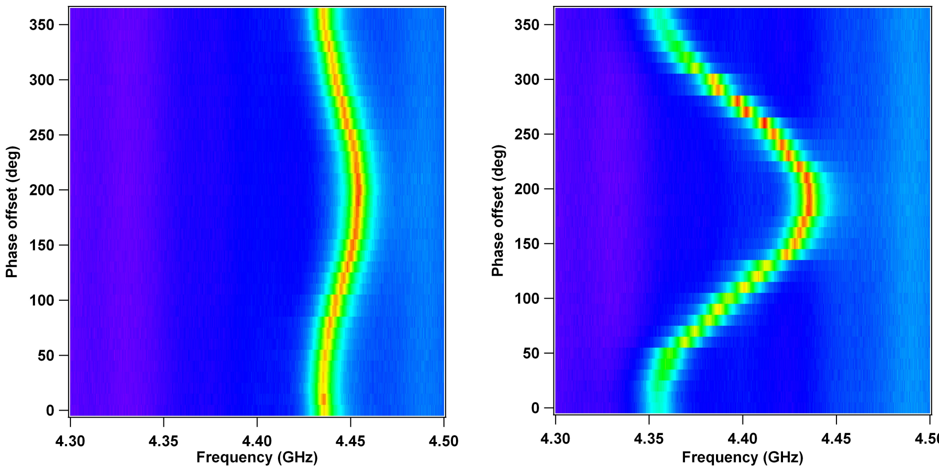

Figure 6.13: The frequency spectrum is probed as a function of phase offset between the two pumps. On the left for a pump power of −25 dBm and on the right for −19 dBm and taking attenuation on the lines into account −62 dBm and −56 dBm. Here the pumping is at three times the resonance frequency.

For the 3ω-pumping case the photon generation of the breathing and translational modes can be seen in Fig. 6.14. The same measurement has been done as for the 2ω-case were for each drive frequency, the power of the applied AC tuning signals and the phase offset between the two signal have been stepped. A comparison to the corresponding 2ω-pumping graphs give that the generation in the 3ω-case is more focused in a smaller area, though the amplitude is higher. As predicted by theory there is a generation of

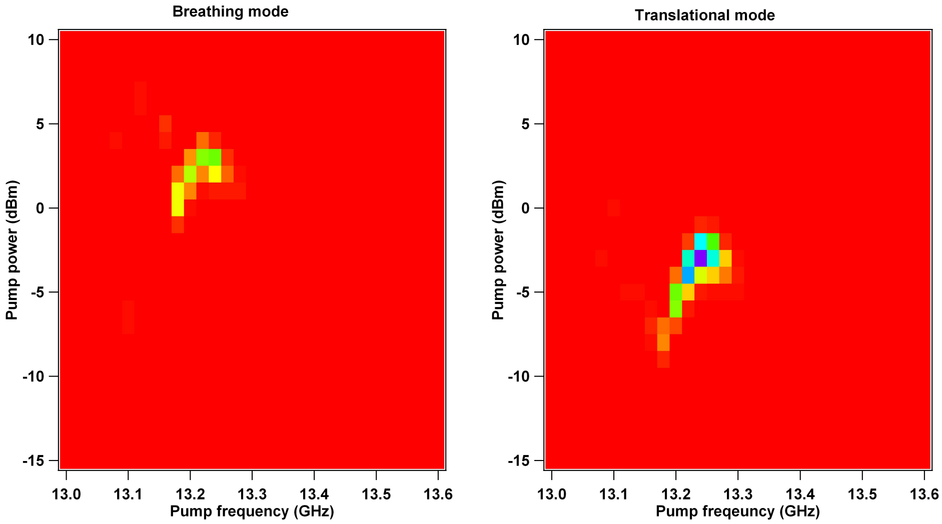

Figure 6.14: In color scale the normalized radiation coming out of the cavity as a function of pump power and frequency for pumping at three times the resonance frequency is shown. On the left for the breathing mode and on the right the translational mode.

photons in the translational mode though there is a smaller one also in the breathing mode. Compared to the 2ω-case where there is a leakage in the translational mode. Remembering that the separation of the energy levels in the resonator is linear and higher modes can be affected by the driving. The generation in "wrong" mode can be due to tuning line-resonator mode coupling. When driving the SQUIDs at three times the resonance frequency one more mode can be affected than when driving at 2ω, which can explain the higher amount of radiation measured in the 3ω-case. Also higher power in the driving was used in the 3ω-case which can contribute to a higher leakage.

7

Conclusion

A $\lambda/2$ resonator with a tunable resonance frequency have been designed, fabricated and measured. The tunability is generated by two SQUIDs, one in each end of the cavity. Static tuning of the resonance frequency has been shown over several periods with both SQUIDs and is working very well. Photons have been generated by high frequency flux modulation under different conditions. It was shown with the phase dependence that both SQUIDs could be addressed. A clear difference could be observed in the breathing mode compared to the translational mode in agreement with theoretical predictions. Although the results are not conclusive this project has been a big step forward.

This was the first experiment performed with a resonator tunable in both ends and therefore conceptual and practical issues have been treated. The outcome of the measurements is difficult to interpret because of the number of unknown parameters. However the results guide us about improvements for future measurements of the dynamical Casimir effect in a doubly tunable resonator. First, the interaction with higher modes needs to be reduced. This can be done by using a resonator with an anharmonic energy spectra, for example a stepped impedance resonator [28].

Another improvement would be to increase the Q-value, *i.e.* decrease the losses. In the resonators fabricated in this thesis the Q-values have been below 1000 in all cases. Previous experiments on tunable resonators have shown Q-values more than 10 times higher. A lower Q-value means that there are more losses that needs to be compensated for in the system before a photon generation can be measured. This might be one of the reasons of the low level on the photon generation in the results. Then what makes this resonator lossy? The SQUIDs may induce losses, when the resonance frequency is tuned away the Q-value decreases.

To further investigate the higher mode interplay in the previous setup a second capacitive probe can be added at the antinode of the second mode. So far the probing of the cavity has been done in the middle, where the odd cavity modes have their maximum value. Hence at this point the even modes have a node. Another approach to probe higher modes is to pump through the probe line, in case of higher mode interaction a shift in resonance frequency should be observed also in the fundamental mode.

Applying the improvements suggested here, measurements of the dynamical Casimir effect using a double tunable cavity can possibly be achieved.

A

Recipe for Cleanroom Fabrication

1. Cleaning - Full wafer
   - $10-15$ min, remover 1165, 60^{o}C
   - ultrasonic bath, 100%, 1 min
   - IPA bath, 2 min circulation
   - QDR bath
   - blowdry
   - ashing 1 min, O_2 plasma
2. Spin resist - Full wafer
   - HDMS primer. 3000 rpm, 1 min, $t_{acc} = 1.5$ s bake 1 min 110^{o}C
   - LOR3B, 3000 rpm, 1 min, $t_{acc} = 1.5$ s bake 5min 200^{o}C
   - S1813, 3000 rpm, 1 min, $t_{acc} = 1.5$ s bake 2 min 110^{o}C
3. Exposure - Full wafer
   - 8.5 s, low-vac mode
4. Development - Full wafer
   - 40 s, MF33319 (lift up after 15 s)
   - QDR bath+blowdry
5. Deposition - Full wafer
   - Ti: 30 Å (2 Å/s) Au: 800 Å (5 Å/s) Pd: 100 Å (2 Å/s)

6. Lift-off - Full wafer
   - remover 1165, 70^oC, 1 h maybe less
   - IPA bath, 2 min circulation
   - QDR bath+blowdry
7. Protection resist - Full wafer
   - S1813, 3000 rpm, 1 min, 1.5 s bake 110^oC 3 min
8. Dicing - Full wafer
   - HVB blade 50 μm
   - tape thickness 75 μm, wafer thickness 380 μm
   - depth of cut 0.950 mm, semidicing 0.725 mm
   - feed rate 3 mm/s
   - spindle speed 35
9. Remove protective resist - Full wafer
   - 1165, 70^oC, rinse with IPA+blowdry
   - ashing 50 W, 1 min
10. Spinning e-beamresist - Full wafer
    - MMA(8.5)EL10 500 rpm, 5 s,$t_{acc} = 2$ s 2000 rpm, 45 s, $t_{acc} = 5$ s bake 5 min, 170^oC
    - ZEP520A 1:1 anisole 3000 rpm, 45 s, $t_{acc} = 0.5$ s bake 5 min 170^oC
11. Develop e-beam resist - Single chips
    - top layer, oxylene 2 min
    - IPA rinsing+blowdry
    - bottom layer, H2O IPA 1:4, 5 min 30 s
    - rinse in IPA
    - blowdry gently!
12. Evaporation plassys - Single chips
    - thicknesses 45 nm+55 nm, oxidation at 0.2 mbar, 30 min, angle $\pm 26.5^o$
13. Lift-off - Single chips
    - remover 1165, 20 min "move" (to get rid of sticking Al) 70^oC
    - rinse in IPA

B

Two Coupled Resonators

In one of the samples the resonator was cut in two parts in the middle. This was done in order to prevent DC currents from flowing through the resonator. Measurements then showed as might be expected that the cut resulted in dividing into two $\lambda/4$ resonators. An avoided level crossing was seen (figure B.1) indicating two coupled resonators. The

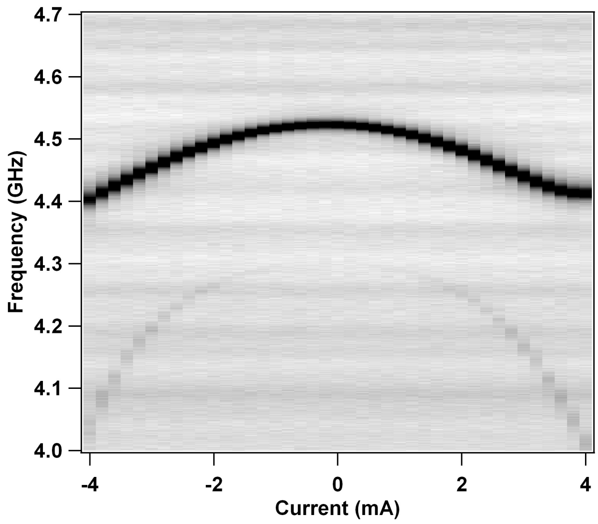

Figure B.1: An avoided level crossing. The two resonances, seen as black and darker grey, corresponds two the two respective resonators. Unfortunately the lower resonance is weak.

two measured frequency modes can be written on the form

$$f^+ = f_m + \sqrt{\Delta^2 + g^2}, \tag{B.1a}$$

$$f^- = f_m - \sqrt{\Delta^2 + g^2}, \tag{B.1b}$$

where Δ denotes the detuning, f_m the center frequency and g the coupling. In detail $\Delta = \frac{f_2 - f_1}{2}$ and $f_m = \frac{f_2 + f_1}{2}$, where in turn f_1 and f_2 are the resonance frequencies of the two separate resonators. Using this model a fit can be obtained as in figure B.2, with a period of 11.79 mA, an offset of 0.12 mA, $L_l/Ll = 7.53 \cdot 10^{-2}$, $f_{10} = 4.48GHz$, $f_{20} = 4.67\,\mathrm{GHz}$ and the coupling $g = 87.3\,\mathrm{GHz}$.

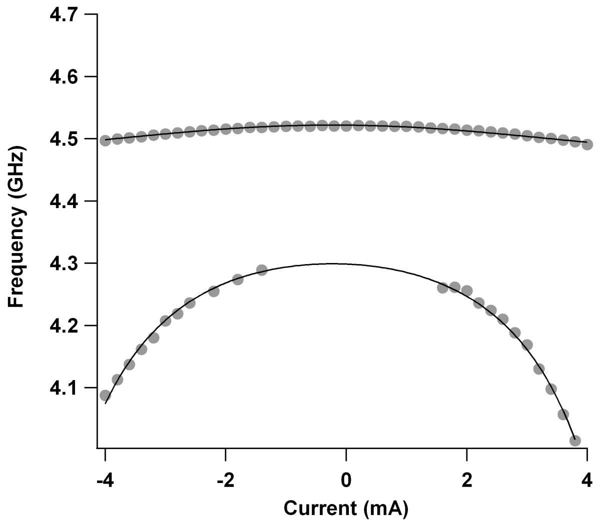

Figure B.2: A fit to the avoided level crossing. Dots corresponds to data and lines to fit.

Bibliography

[1] C. M. Wilson, G. Johansson, A. Pourkabirian, M. Simoen, J. R. Johansson, T. Duty, F. Nori, and P. Delsing. Observation of the dynamical casimir effect in a superconducting circuit. *Nature*, 479:376–379, November 2011.

[2] Jeong-Young Ji, Hyun-Hee Jung, and Kwang-Sup Soh. Interference phenomena in the photon production between two oscillating walls. *Phys. Rev. A*, 57(6):4952–4955, June 1998.

[3] A. Lambrecht, M. T. Jaekel, and S. Reynaud. Frequency up-converted radiation from a cavity moving in vacuum. *The European Physical Journal D - Atomic, Molecular, Optical and Plasma Physics*, 3, 1998.

[4] D. A. R. Dalvit and F. D. Mazzitelli. Creation of photons in an oscillating cavity with two moving mirrors. *Phys. Rev. A*, 59:3049–3059, Apr 1999.

[5] H. B. G. Casimir. On the attraction between two perfectly conducting plates. In *Proceedings of the Royal Netherlands Academy of Arts and Sciences*, 51, pages 793–795, 1948.

[6] C. C. Gerry and P. L. Knight. *Introductory Quantum Optics*. Cambridge University Press, 2008.

[7] J. R. Johansson, G. Johansson, C. M. Wilson, and F. Nori. Dynamical casimir effect in superconducting microwave circuits. *Phys. Rev. A*, 82(5):052509, November 2010.

[8] G. T. Moore. Quantum Theory of the Electromagnetic Field in a Variable-Length One-Dimensional Cavity. *Journal of Mathematical Physics*, 11:2679–2691, September 1970.

[9] S. A. Fulling and P. C. W. Davies. Radiation from a moving mirror in two dimensional space-time: Conformal anomaly. *Proceedings of the Royal Society of London. A. Mathematical and Physical Sciences*, 348(1654), 1976.

[10] M. Sandberg, C. M. Wilson, F. Persson, T. Bauch, G. Johansson, V. Schumeiko, T. Duty, and P. Delsing. Tuning the field in a microwave resonator faster than the photon lifetime. *Applied Physics Letters*, 92:203501, May 2008.

[11] C. M. Wilson, T. Duty, M. Sandberg, F. Persson, V. Shumeiko, and P. Delsing. Photon generation in an electromagnetic cavity with a time-dependent boundary. *Phys. Rev. Lett.*, 105(23):233907, Dec 2010.

[12] J. R. Johansson, G. Johansson, C. M. Wilson, and F. Nori. Dynamical casimir effect in a superconducting coplanar waveguide. *Phys. Rev. Lett.*, 103:147003, Sep 2009.

[13] K. H. Onnes. The superconductivity of mercury. Technical report, Comm. Phys. Lab. Univ. Leiden, 1911.

[14] J. R. Waldram. *Superconductivity of Metals and Cuprates*. Institute of Physics Publishing, 1996.

[15] B. D. Josephson. Possible new effects in superconductive tunneling. *Physics Letters*, June 1962.

[16] T. Van Duzer and C. W. Turner. *Principles of Superconductive Devices and Circuits*. Prentice Hall PTR, 1999.

[17] F. London and H. London. The electromagnetic equations of the supraconductor. *Proceedings of the Royal Society of London. Series A, Mathematical and Physical Sciences*, 149(866):pp. 71–88, 1935.

[18] D. M. Pozar. *Microwave Engineering 3rd edition*. Wiley, 2005.

[19] C.P. Wen. Coplanar waveguide: A surface strip transmission line suitable for nonreciprocal gyromagnetic device applications. *Microwave Theory and Techniques, IEEE Transactions on*, 17(12), December 1969.

[20] M. Sandberg. *Fast-tunable resonators and quantum electrical circuits*. PhD thesis, Chalmers university of technology, 2009.

[21] M. I. Dykman, C. M. Maloney, V. N. Smelyanskiy, and M. Silverstein. Fluctuational phase-flip transitions in parametrically driven oscillators. *Phys. Rev. E*, 57:5202–5212, May 1998.

[22] C. M. Wilson, T. Duty, and P. Delsing. Parametric oscillators based on superconducting circuits. An unpublished book chapter.

[23] M. Göppl, A. Fragner, M. Baur, R. Bianchetti, S. Filipp, J. M. Fink, P. J. Leek, G. Puebla, L. Steffen, and A. Wallraff. Coplanar waveguide resonators for circuit quantum electrodynamics. *Journal of Applied Physics*, 104(11), December 2008.

[24] D. Gunnarsson K. Bladh, T. Duty and P. Delsing. The single cooper-pair box as a charge qubit. *New Journal of Physics*, August 2005.

[25] P Krantz. Investigation of transmon qubit designs -a study of plasma frequency predictability. Master thesis at Chalmers University of Technology, 2010.

[26] S.S. Gevorgian, T. Martinsson, P.L.J. Linner, and E.L. Kollberg. Cad models for multilayered substrate interdigital capacitors. *Microwave Theory and Techniques, IEEE Transactions on*, 44(6), June 1996.

[27] D. K. Cheng. *Fundamentals of Engineering Electromagnetics.* Addison-Wesley Publishing company, 1993.

[28] M. Sagawa, M. Makimoto, and S. Yamashita. Geometrical structures and fundamental characteristics of microwave stepped-impedance resonators. *Microwave Theory and Techniques, IEEE Transactions on*, 45, July 1997.